

TAKING A STEP BACK WITH KCAL: MULTI-CLASS KERNEL-BASED CALIBRATION FOR DEEP NEURAL NETWORKS

Zhen Lin

University of Illinois at Urbana-Champaign
Urbana, IL 61801
zhenlin4@illinois.edu

Shubhendu Trivedi

shubhendu@csail.mit.edu

Jimeng Sun

University of Illinois at Urbana-Champaign
Urbana, IL 61801
jimeng@illinois.edu

ABSTRACT

Deep neural network (DNN) classifiers are often overconfident, producing miscalibrated class probabilities. In high-risk applications like healthcare, practitioners require *fully calibrated* probability predictions for decision-making. That is, conditioned on the prediction *vector*, *every* class’ probability should be close to the predicted value. Most existing calibration methods either lack theoretical guarantees for producing calibrated outputs, reduce classification accuracy in the process, or only calibrate the predicted class. This paper proposes a new Kernel-based calibration method called KCal. Unlike existing calibration procedures, KCal does not operate directly on the logits or softmax outputs of the DNN. Instead, KCal learns a metric space on the penultimate-layer latent embedding and generates predictions using kernel density estimates on a calibration set. We first analyze KCal theoretically, showing that it enjoys a provable *full* calibration guarantee. Then, through extensive experiments across a variety of datasets, we show that KCal consistently outperforms baselines as measured by the calibration error and by proper scoring rules like the Brier Score.

1 INTRODUCTION

The notable successes of Deep Neural Networks (DNNs) in complex classification tasks, such as object detection (Ouyang & Wang, 2013), speech recognition (Deng et al., 2013), and medical diagnosis (Qiao et al., 2020; Biswal et al., 2017), have made them essential ingredients within various critical decision-making pipelines. In addition to the classification accuracy, a classifier should ideally also generate reliable uncertainty estimates represented in the predicted probability vector. An influential study (Guo et al., 2017) reported that modern DNNs are often overconfident or *miscalibrated*, which could lead to severe consequences in high-stakes applications such as healthcare (Jiang et al., 2012).

Calibration is the process of closing the gap between the prediction and the ground truth distribution given this prediction. For a K -class classification problem, with covariates $X \in \mathcal{X}$ and the label $Y \in \mathcal{Y} = [K]$, denote our classifier $\mathcal{X} \mapsto \Delta^{K-1}$ as $\hat{\mathbf{p}} = [\hat{p}_1, \dots, \hat{p}_K]$, where Δ^{K-1} is the $(K-1)$ -simplex. Then,

Definition 1. (*Full Calibration (Kull et al., 2019; Vaicenavicius et al., 2019)*) $\hat{\mathbf{p}}$ is *fully-calibrated* if $\forall k \in [K]$:

$$\forall \mathbf{q} = [q_1, \dots, q_K] \in \Delta^{K-1}, \mathbb{P}\{Y = k | \hat{\mathbf{p}}(X) = \mathbf{q}\} = q_k. \quad (1)$$

It is worth noting that Def. (1) implies *nothing about accuracy*. In fact, ignoring X and simply predicting π , the class frequency vector, results in a fully calibrated but inaccurate classifier. As a result, our goal is always to improve calibration *while maintaining accuracy*. Another important requirement is that $\hat{\mathbf{p}} \in \Delta^{K-1}$. Many binary calibration methods such as Zadrozny & Elkan (2001; 2002) result in vectors that are not interpretable as probabilities, and have to be normalized.

Many existing works only consider *confidence calibration* (Guo et al., 2017; Zhang et al., 2020; Wenger et al., 2020; Ma & Blaschko, 2021), a much weaker notion than that encapsulated by Def. (1) and only calibrates the predicted class (Kull et al., 2019; Vaicenavicius et al., 2019).

Definition 2. (*Confidence Calibration*) $\hat{\mathbf{p}}$ is confidence-calibrated if:

$$\forall q \in [0, 1], \mathbb{P}\{Y = \arg \max_k \hat{p}_k(X) \mid \max_k \hat{p}_k(X) = q\} = q. \quad (2)$$

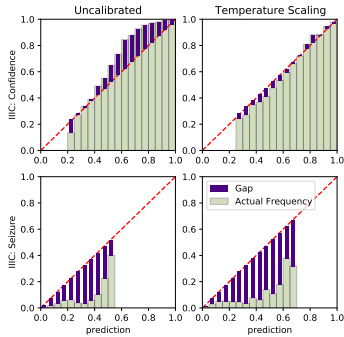


Figure 1: Reliability diagrams for confidence calibration (top) and Seizure (bottom). The popular temperature scaling (right) only calibrates the confidence, leaving Seizure poorly calibrated. See Figure 2 and the Appendix for complete reliability diagrams.

However, confidence calibration is far from sufficient. Doctors need to perform differential diagnoses on a patient, where multiple possible diseases should be considered with proper probabilities for all of them, not only the most likely diagnosis. Figure 1 shows an example where the confidence is calibrated, but prediction for important classes like Seizure is poorly calibrated. A classifier can be confidence-calibrated but not useful for differential diagnoses if the probability assignments for most diseases are inaccurate.

Recent research effort has started to focus on full calibration, for example, in Vaicenavicius et al. (2019); Kull et al. (2019); Widmann et al. (2019); Karandikar et al. (2021); Mukhoti et al. (2020); Patel et al. (2021). We approach this problem by leveraging the latent neural network embedding in a nonparametric manner. Nonparametric methods such as histogram binning (HB) (Zadrozny & Elkan, 2001) and isotonic regression (IR) (Zadrozny & Elkan, 2002), are natural for calibration and have become popular. Gupta & Ramdas (2021) recently showed a calibration guarantee for HB. However, HB usually leads to noticeable drops in accuracy (Patel et al., 2021), and IR is prone to overfitting (Niculescu-Mizil & Caruana, 2005). Unlike existing methods, we take one step back and train a new low-dimensional metric space on the penultimate-layer embeddings of DNNs. Then, we use a kernel density estimation-based classifier to predict the class probabilities directly. We refer to our **Kernel-based Calibration** method as KCal. Unlike most calibration methods, KCal provides high probability error bounds for *full calibration* under standard assumptions. Empirically, we show that with little overhead, KCal outperforms all existing calibration methods in terms of calibration quality, across multiple tasks and DNN architectures, while maintaining and sometimes improving the classification accuracy.

Summary of Contributions:

- We propose KCal, a principled method that calibrates DNNs using kernel density estimation on the *latent embeddings*.
- We present an efficient pipeline to train KCal, including a dimension-reducing projection and a stratified sampling method to facilitate efficient training.
- We provide finite sample bounds for the calibration error of KCal-calibrated output under standard assumptions. To the best of our knowledge, this is the first method with a full calibration guarantee.
- In extensive experiments on multiple datasets and state-of-the-art models, we found that KCal outperforms existing calibration methods in commonly used evaluation metrics. We also show that KCal provides more reliable predictions for important classes in the healthcare datasets.

The code to replicate all our experimental results is submitted along with supplementary materials.

2 RELATED WORK

Research on calibration originated in the context of meteorology and weather forecasting (see Murphy & Winkler (1984) for an overview) and has a long history, much older than the field of machine

learning (Brier, 1950; Murphy & Winkler, 1977; Degroot & Fienberg, 1983). We refer to Filho et al. (2021) for a holistic overview and focus below on methods proposed in the context of modern neural networks. Based on underlying methodological similarities, we cluster them into distinct categories.

Scaling: A popular family of calibration methods is based on scaling, in which a mapping is learned from the predicted logits to probability vectors. Confidence calibration scaling methods include temperature scaling (TS) (Guo et al., 2017) and its antecedent Platt scaling (Platt, 1999), an ensemble of TS (Zhang et al., 2020), Gaussian-Process scaling (Wenger et al., 2020), combining a base calibrator (TS) with a rejection option (Ma & Blaschko, 2021). Matrix scaling with regularization was also used to perform full calibration (Kull et al., 2019). While some scaling-based methods can be data-efficient, there are no known theoretical guarantees for them to the best of our knowledge.

Binning: Another cluster of solutions relies on binning and its variants, and includes uniform-mass binning (Zadrozny & Elkan, 2001), scaling before binning (Kumar et al., 2019), and mutual-information-maximization-based binning (Patel et al., 2021). Isotonic regression (Zadrozny & Elkan, 2002) is also often interpreted as binning. Uniform-mass binning (Zadrozny & Elkan, 2001) has a distribution-free finite sample calibration guarantee (Gupta & Ramdas, 2021) and asymptotic convergent ECE estimation (Vaicenavicius et al., 2019). However, in practice, binning tends to decrease accuracy (Patel et al., 2021; Guo et al., 2017). Binning can also be considered a member of the broader nonparametric calibration family of methods. Such methods also include Gaussian Process Calibration (Wenger et al., 2020), which however also only considers confidence calibration.

Loss regularization: There are also attempts to train a calibrated DNN to begin with. Such methods typically add a suitable regularizer to the loss function (Karandikar et al., 2021; Mukhoti et al., 2020; Kumar et al., 2018), which can sometimes result in expensive optimization and reduction in accuracy.

Use of Kernels: Although not directly used for calibration, kernels have also been used for uncertainty quantification for deep learning classification. In classification with rejection, the k-nearest-neighbors algorithm (kNN), closely related to kernel-based methods, has been used to provide a “confidence measure” which is used to make a binary decision (i.e., whether to reject or to predict) (Papernot & McDaniel, 2018; Jiang et al., 2018). Recently, continuous kernels have also been used to measure calibration quality or used as regularization during training (Widmann et al., 2019; Kumar et al., 2018). Zhang et al. (2020) introduced a kernel density estimation (KDE) proxy estimator for estimating ECE. However, it uses a un-optimized kernel over Δ^{K-1} , and shows the KDE-ECE estimator (but not the calibration map) is consistent. To the best of our knowledge, use of trained KDE to calibrate predictions hasn’t been proposed before. Further, we also provide a bound on the calibration error.

3 KCAL: KERNEL-BASED CALIBRATION

In this section, we formally introduce KCal, study its calibration properties theoretically, and present crucial implementation details and comparisons with other methods. Specifically, in Section 3.1, we discuss how to construct (automatically) calibrated predictions for test data using a calibration set \mathcal{S}_{cal} . Doing so requires a well-trained kernel and metric space, and we describe a procedure to train such a kernel in Section 3.2. In Section 3.3, we show that an appropriate shrinkage rate of the bandwidth ensures that the KCal prediction is automatically calibrated. Sections 3.4 provides implementation details. Finally, in Section 3.5, we compare and contrast KCal with existing methods.

3.1 CLASSIFICATION WITH KERNEL DENSITY ESTIMATION

Following the calibration literature, we first require a holdout calibration set $\mathcal{S}_{\text{cal}} = \{X_i, Y_i\}_{i=1}^N$. In KCal, we fix a kernel function $\hat{\phi}$ which is learned (the learning procedure is described in Section 3.2). For a new datum X_{N+1} , the class probability $\hat{\mathbf{p}}_k(X_{N+1})$ takes the following form:

$$\hat{\mathbf{p}}_k(X_{N+1}; \hat{\phi}, \mathcal{S}_{\text{cal}}) = \frac{\sum_{(x,y) \in \mathcal{S}_{\text{cal}}^k} \hat{\phi}(x, X_{N+1})}{\sum_{(x,y) \in \mathcal{S}_{\text{cal}}} \hat{\phi}(x, X_{N+1})}, \quad (3)$$

where $\mathcal{S}_{\text{cal}}^k := \{(x, y) \in \mathcal{S}_{\text{cal}} | y = k\}$. The notation $\hat{\mathbf{p}}_k(X_{N+1}; \hat{\phi}, \mathcal{S}_{\text{cal}})$ emphasizes the dependence on $\hat{\phi}$ and \mathcal{S}_{cal} . However, we will use $\hat{\mathbf{p}}_k(X_{N+1})$ when the dependence is clear from context.

Remarks: What we have described is essentially the classical nonparametric procedure of applying kernel density estimation for classification. For a moment, suppose we know the true density function

f_k of \mathcal{P}_k (the distribution of all the data in class k), and the proportion of class k , denoted π_k (such that $\sum_{k \in [K]} \pi_k = 1$). Then, for any particular x_0 , using the Bayes rule we get:

$$\mathbb{P}\{Y = k|X = x_0\} = \frac{f_k(x_0)\pi_k}{\sum_{k' \in [K]} f_{k'}(x_0)\pi_{k'}}. \quad (4)$$

Now, replacing f_k with the kernel density estimate $\hat{f}_k(x_0) := (\sum_{(x,y) \in \mathcal{S}_{\text{cal}}^k} \hat{\phi}_b(x, x_0))/|\mathcal{S}_{\text{cal}}^k|$, and the class proportion π_k with $\hat{\pi}_k := |\mathcal{S}_{\text{cal}}^k|/|\mathcal{S}_{\text{cal}}|$ we get back Eq. (3).

3.2 TRAINING

Employing an appropriate kernel function $\hat{\phi}$ is crucial for good performance under the kernel density framework. The kernel in turn has a critical reliance on the choice of the underlying metric. To obtain good performance using deep learning learning models, we train a metric space on top of the penultimate layer embeddings.

To begin, we assume a deep neural network is already trained on $\mathcal{S}_{\text{train}} = \{X_i^{\text{train}}, Y_i^{\text{train}}\}_{i=1}^M$. We place no limitations on the form of loss function, optimizer, or the model architecture. However, we do require the neural net to compute an embedding before a final prediction layer, which is always the case in modern classification models. We denote the embedding function from $\mathcal{X} \mapsto \mathbb{R}^h$ as \mathbf{f} .

Given a base ‘‘mother kernel’’ function ϕ , such as the Radial Basis Function (RBF) kernel, we denote the kernel with bandwidth b as $\phi_b := \frac{1}{b}\phi(\frac{\cdot}{b})$. We parameterize the learnable kernel as:

$$\hat{\phi}(x, x') := \hat{\phi}_{\mathbf{\Pi}, \mathbf{f}, b}(x, x') := \phi_b(\mathbf{\Pi}(\mathbf{f}(x)) - \mathbf{\Pi}(\mathbf{f}(x'))). \quad (5)$$

where $\mathbf{\Pi} : \mathbb{R}^h \mapsto \mathbb{R}^d$ is a dimension-reducing projection parameterized by a shallow MLP (Section 3.4). Since the inference time is linear in d , letting $d < h$ also affords computational benefits.

Given that the embedding function $\mathbf{f}(x)$ from the neural network is fixed, the only learnable entities are b and $\mathbf{\Pi}$. In the training phase, we fix $b = 1$, and train $\mathbf{\Pi}$ using (stochastic) gradient descent and log-loss. The specific value of b does not matter since it can be folded into $\mathbf{\Pi}$. Let us denote $\mathcal{S}_{\text{train}}^k = \{(x, y) \in \mathcal{S}_{\text{train}} : y = k\}$. In each iteration, we randomly sample two batches of data from $\mathcal{S}_{\text{train}}$ - the prediction data, denoted as $\mathcal{S}_{\text{train}}^B$, to evaluate $\mathbf{\Pi}$, and ‘‘background’’ data for each k , denoted as \mathcal{B}^k , from $\mathcal{S}_{\text{train}}^k \setminus \mathcal{S}_{\text{train}}^B$ to construct the KDE classifier. Then, the prediction for any x_j is given by

$$\hat{\mathbf{p}}_k(x_j; \hat{\phi}, \mathcal{S}_{\text{train}} \setminus \mathcal{S}_{\text{train}}^B) := \frac{\sum_{(x,y) \in \mathcal{B}^k} \frac{|\mathcal{S}_{\text{train}}^k \setminus \mathcal{S}_{\text{train}}^B|}{|\mathcal{B}^k|} \hat{\phi}(x, x_j)}{\sum_{k', (x,y) \in \mathcal{B}^{k'}} \frac{|\mathcal{S}_{\text{train}}^{k'} \setminus \mathcal{S}_{\text{train}}^B|}{|\mathcal{B}^{k'}|} \hat{\phi}(x, x_j)} \quad (6)$$

where $\hat{\phi}$ is shorthand for $\hat{\phi}_{\mathbf{\Pi}, \mathbf{f}, b=1}$ defined in Eq. (5). The log-loss is given formally by

$$L = -\frac{1}{B} \sum_{(x,y) \in \mathcal{S}_{\text{train}}^B} \log \hat{\mathbf{p}}_y(x; \hat{\phi}_{\mathbf{\Pi}, \mathbf{f}, 1}, \mathcal{S}_{\text{train}} \setminus \mathcal{S}_{\text{train}}^B). \quad (7)$$

Finally, we pick a $b = b^*$ on the calibration set \mathcal{S}_{cal} using cross-validation. This is because b should be chosen contingent on the sample size (Section 3.3). Choosing b can be done efficiently (Section 3.4). Algorithm 1 summarizes the steps we explicated upon so far.

3.3 THEORETICAL ANALYSIS: CALIBRATION COMES FREE

In the previous section, we have only described a procedure to improve the prediction accuracy for $\hat{\mathbf{p}}$ on $\mathcal{S}_{\text{train}}$. This section will show that calibration comes free with the $\hat{\mathbf{p}}$ obtained using Algorithm 1. In particular, we show that as the sample-size for each class in \mathcal{S}_{cal} increases, $\hat{\mathbf{p}}$ converges to the true frequency vector of Y given the input. In interest of smoother presentation, we only state the relevant claims in what follows. Detailed proofs are presented in the Appendix.

To begin, we make a few standard assumptions, such as in Chac3n & Duong (2018), including:

- ($\forall k$) The density on the embedded space, $\mathbf{\Pi}(\mathbf{f}(\mathcal{X}|Y = k))$, denoted as $f_{\mathbf{\Pi} \circ \mathbf{f}, k}$, is square integrable and twice differentiable, with all second order partials bounded, continuous, and square integrable.
- ϕ is spherically symmetric, with a finite second moment.

Lemma 3.1 and 3.2 focus on an arbitrary class k and ignore the subscript k to the density f for readability. We denote the size $|\mathcal{S}_{\text{cal}}^k| = m$. Intuitively, due to the bias-variance trade-off, a suitable bandwidth b will depend on m : A small b reduces bias, but with the finite m , a smaller b also leads to increased variance. Thus, b should go to 0 “slowly”, which is formally stated below:

Lemma 3.1. *For almost all x , if $b^d m \rightarrow \infty$ and $b \rightarrow 0$ as $m \rightarrow \infty$, then we have*

$$\|\hat{f}_{\Pi \circ f, k}(x) - f_{\Pi \circ f, k}(x)\|_2 \xrightarrow{P} 0 \text{ as } m \rightarrow \infty. \quad (8)$$

Here $\hat{f}_{\Pi \circ f, k}$ is the estimated $f_{\Pi \circ f, k}$ using \mathcal{S}_{cal} . Recall that d is the dimension of $\Pi(\mathbf{f}(\mathcal{X}))$. We will call such a bandwidth b *admissible*, and we sometimes write $b(m)$ to emphasize the dependence on m . The following lemma gives the optimal admissible bandwidth:

Lemma 3.2. *The optimal bandwidth is $b = \Theta(m^{-\frac{1}{d+4}})$, which leads to the fastest decreasing MSE (i.e. $\mathbb{E}[\|\hat{f}_{\Pi \circ f, k}(x) - f_{\Pi \circ f, k}(x)\|_2]$) of $O(m^{-\frac{4}{d+4}})$.*

Now we are in a position to present the main theoretical results. In the following, m denotes the rarest class’s count ($m := \min_k \{|\mathcal{S}_{\text{cal}}^k|\}$). Theorem 3.3 provides a bound between $\hat{\mathbf{p}}$ and the true conditional probability vector on the embedded space $\mathbf{p}(\Pi(\mathbf{f}(X)))$:

Theorem 3.3. *Fixing x such that the density of $\Pi(\mathbf{f}(x))$ is positive, with $b(m) = \Theta(m^{-\frac{1}{d+4}})$, for any $\lambda \in (0, 2)$:*

$$\mathbb{P}\{|\hat{\mathbf{p}}_k(x) - \mathbf{p}_k(\Pi(\mathbf{f}(x)))| > (3K + 1)Cm^{-\frac{\lambda}{d+4}}\} \leq Ke^{-Bm^{\frac{4-2\lambda}{d+4}}} \quad (9)$$

$$\text{where } \mathbf{p}_k(\Pi(\mathbf{f}(x))) := \mathbb{P}\{Y = k | \Pi(\mathbf{f}(X)) = \Pi(\mathbf{f}(x))\} \quad (10)$$

for some constant B and C . As a corollary, $\hat{\mathbf{p}}(x) \xrightarrow{\text{almost surely}} \mathbf{p}(\Pi(\mathbf{f}(x)))$ as $m \rightarrow \infty$.

Next, we bound the full calibration error with additional standard assumptions. More specifically, we use and build upon the main uniform convergence result for classical KDE presented in Jiang (2017), to obtain Theorem 3.4:

Theorem 3.4. *Assume $f_{\Pi \circ f, k}$ is α -Hölder continuous and bounded away from 0 for any k . For an admissible $b(m)$ with shrinkage rate $\Theta((\frac{\log m}{m})^{\frac{1}{d+2\alpha}})$, for some constants B and C we have:*

$$\mathbb{P}\{\sup_{X, k} |\hat{\mathbf{p}}_k(X) - \mathbb{P}\{Y = k | \hat{\mathbf{p}}(X)\}| > (3K + 1)C(\frac{\log m}{m})^{\frac{\alpha}{d+2\alpha}}\} \leq K(m^{-1} + m^{-B\frac{2\alpha}{d+2\alpha}} m^{\frac{d}{d+2\alpha}}). \quad (11)$$

We now proceed to present details pertaining to the efficient implementation of KCal.

3.4 IMPLEMENTATION TECHNIQUES

Efficient Training: As might be immediately apparent, utilizing algorithm 1 for prediction using full $\mathcal{S}_{\text{train}} \setminus \mathcal{S}_{\text{train}}^B$ can be an expensive exercise. In order to afford a training speedup, we consider a random subset from $\mathcal{S}_{\text{train}} \setminus \mathcal{S}_{\text{train}}^B$ using a modified stratified sampling. Specifically, we take m random samples from each $\mathcal{S}_{\text{train}}^k$, denoted as $\mathcal{S}_{\text{train}}^{k, m}$, and replace the right-hand side of Eq. 6 with:

$$\frac{\sum_{(x, y) \in \mathcal{S}_{\text{train}}^{k, m}} \frac{|\mathcal{S}_{\text{train}}^k|}{m} \hat{\phi}(x, x_0)}{\sum_{k' \in [K], (x, y) \in \mathcal{S}_{\text{train}}^{k', m}} \frac{|\mathcal{S}_{\text{train}}^{k'}|}{m} \hat{\phi}(x, x_0)}. \quad (12)$$

The re-scaling term $\frac{|\mathcal{S}_{\text{train}}^k|}{m}$ is crucial to get an unbiased estimate of $\hat{f}_k \hat{\pi}_k$. The stratification employed makes the training more stable, while also reducing the estimation variance for rarer classes (more details in Appendix B). The overall complexity is now $O(KmdhB)$ per batch. In all experiments, we used $m = 20$ and $B = 64$.

Form of Π : While there is considerable freedom in choosing a suitable form for Π , we parameterize Π with a two layer MLP with a skip connection. Consequently, Π can reduce to linear projection when sufficient, and be more expressive when necessary. We also experimented with using only a linear projection, the results for which are included in the appendix. We fix the output dimension to $d = \min\{\dim(\mathbf{f}), 32\}$, except for ImageNet ($d = 128$).

Algorithm 1 Overview of KCal**Input:** $\mathcal{S}_{\text{train}}: \{(X_i^{\text{train}}, Y_i^{\text{train}})\}_{i=1}^M$ used to train the NN $\mathcal{S}_{\text{cal}}: \{(X_i, Y_i)\}_{i=1}^N$ calibration set f : Embedding function $\mathcal{X} \rightarrow \mathbb{R}^h$ (trained NN) X_{N+1} : Unseen datum for prediction**Training (of the projection Π):**Denote $\mathcal{S}_{\text{train}}^k := \{(x, y) \in \mathcal{S}_{\text{train}} | y = k\}$.Denote ϕ_b as a base kernel function (e.g. RBF) with bandwidth b .**repeat**Sample $\mathcal{S}_{\text{train}}^B = \{(x_j, y_j)\}_{j=1}^B$ from $\mathcal{S}_{\text{train}}$.Compute $\hat{\mathbf{p}}(x_j)$ via Eq. (6).Loss $l \leftarrow \frac{1}{B} \sum_{j=1}^B \text{LogLoss}(\hat{\mathbf{p}}(x_j), y_j)$.Update Π with (stochastic) gradient descent.**until** the loss l does not improve.Set $\hat{\phi}_b \leftarrow \hat{\phi}_{\Pi, f, b}$ for inference.**Inference:**Denote $\mathcal{S}_{\text{cal}}^k := \{(x, y) \in \mathcal{S}_{\text{cal}} | y = k\}$.Tune b^* on \mathcal{S}_{cal} by minimizing log loss.

$$\hat{\mathbf{p}}_k(X_{N+1}) \leftarrow \frac{\sum_{(x, y) \in \mathcal{S}_{\text{cal}}^k} \hat{\phi}_{b^*}(x, X_{N+1})}{\sum_{(x, y) \in \mathcal{S}_{\text{cal}}} \hat{\phi}_{b^*}(x, X_{N+1})}.$$

Employing a KDE classifier (KCal) with linear models trained in various ways, after mapping all the data with f . Note that this characterization is true for most existing methods, with a few exceptions (e.g., those summarized under “loss regularization” in Section 2).

Employing a KDE classifier affords some clear advantages such as a straightforward convergence guarantee and some interpretability¹. Furthermore, KCal can also be improved in an online fashion, a benefit especially desirable in certain high-stakes applications such as in healthcare. For example, a hospital can calibrate a trained model prior to deployment using its own patient data (which is usually not available to train the original model) as it becomes available.

Another important advantage of KCal is concerning normalization. In fact, simultaneously calibrating all classes while satisfying the constraint that $\hat{\mathbf{p}} \in \Delta^{K-1}$ is a distinguishing challenge for multi-class calibration. Many calibration methods perform one-vs-rest calibration for each class, and require a separate normalization step at test time (Zadrozny & Elkan, 2001; 2002; Patel et al., 2021; Gupta et al., 2021). This creates a gap between training and testing and could lead to drastic drop in performance (Section 4). On the other hand, KCal automatically satisfies $\hat{\mathbf{p}} \in \Delta^{K-1}$, and the normalization is consistent during training and testing.

A disadvantage of KCal is the need to remember the $\Pi(f(\mathcal{S}_{\text{cal}}))$ used to generate the KDE prediction. This is however mitigated to a large extent by the dimension reduction step, which already reduces the computational overhead significantly². For example, in one of our experiments on CIFAR-100, there are 160K (5K images, $d = 32$) scalars to remember, which is only 0.2% of the parameters (85M+) of the original DNN (ViT-base-patch16). Moreover, KDE inference is trivial to parallelize on GPUs. There is also a rich, under-explored, literature to further speed up the inference. Examples include, KDE merging (Sodkomkham et al., 2016), Dual-Tree (Gray & Moore, 2003), and Kernel Herding (Chen et al., 2010). These methods can easily be used in conjunction with KCal.

4 EXPERIMENTS

4.1 DATA AND NEURAL NETWORKS

We utilize two sets of data: computer vision benchmarks on which previous calibration methods were tested, and health monitoring datasets where *full* calibration is crucial for diagnostic applications. Table 1 summarizes the datasets and their splits.

¹That is, one could understand how the prediction is made by examining similar samples.

²Experiments about the effect of d on performance and overhead are provided in the Appendix.

Bandwidth Selection: Finally, to find the optimal bandwidth using \mathcal{S}_{cal} , we use Golden-Section search (Kiefer, 1953) to find the log-loss-minimizing b^* . This takes $O(\log \frac{ub-lb}{tol})$ steps where $[lb, ub]$ is the search space, and tol is the tolerance. Essentially, we assume that the loss is a convex function with respect to b , permitting an efficient search (see Appendix H, which presents empirical evidence that the convexity assumption is valid across datasets).

3.5 COMPARISONS WITH EXISTING CALIBRATION METHODS

Most existing calibration methods discussed in Section 2 and KCal all utilize a holdout calibration set. However, unlike KCal, existing works usually fix the last neural network layer. KCal, on the other hand, “takes a step back”, and replaces the last prediction layer with a kernel density estimation based classifier. Since the DNN f is fixed regardless of whether we use the original last layer or not, we are really compar-

Table 1: Dataset summary: Splits and number of classes (K).

Dataset	IIC	IIC(pat)	ISRUC	ISRUC(pat)	PN2017	C10	C100	SVHN	ImageNet
Train	103,818	1,936	61,841	69	15,087	45,000,	45,000	65,931	1,281,167
Calibration	1,787	77	1,372	6	253	5,000	5,000	7,326	25,000
Test	33,953	684	26,070	24	4,813	10,000	10,000	26,032	25,000
K	6	6	5	5	4	10	100	10	1,000

Benchmark data Following Kull et al. (2019), we use multiple image benchmark datasets, including CIFAR-10, CIFAR-100, and SVHN (Krizhevsky, 2009; Netzer et al., 2011). We reserve 10% of the training data as the calibration set. We fine-tune pretrained ViT (Dosovitskiy et al., 2021) and MLP-Mixer (Mixer) (Tolstikhin et al., 2021) from the `timm` library (Wightman, 2019). We chose ViT and Mixer because they are the state-of-the-art neural architectures in computer vision, and accuracy should come before calibration quality. We also included the ImageNet dataset (Deng et al., 2009) and use the pretrained Inception ResNet V2 (Szegedy et al., 2017) following Patel et al. (2021).

Health monitoring data We also use three health monitoring datasets for diagnostic tasks: IIC (Jing et al., 2021), an ictal-interictal-injury-continuum (IIC) patterns classification dataset; ISRUC (Khalighi et al., 2016), a sleep staging (classification) dataset using polysomnographic (PSG) recordings; PN2017 (2017 PhysioNet Challenge) (Clifford et al., 2017; Goldberger et al., 2000), a public electrocardiogram (ECG) dataset for rhythm (particularly Atrial Fibrillation) classification. For the training set, we follow Hong et al. (2019); Jing et al. (2021) for PN2017 and IIC, and used 69 patients’ data for ISRUC. For the remaining data, 5% is used as the calibration set and 95% for testing. We perform additional experiments after splitting into training/calibration/test sets by patients for IIC and ISRUC³, marked as the “pat” version in tables. The calibration/test split is 20/80 in “IIC (pat)” and “ISRUC (pat)” because the number of patients is small. For IIC and ISRUC, we follow the standard practice and train a CNN (ResNet) on the spectrogram (Biswal et al., 2017; Ruffini et al., 2019; Yuan et al., 2019). For PN2017, we used a top-performing model from the 2017 PhysioNet Challenge, MINA (Hong et al., 2019).

Table 2: Accuracy in % (\uparrow means higher=better). Accuracy numbers lower than the uncalibrated predictions are in **dark red** and the best are in **bold** (both at $p=0.01$). KCal typically improves or maintains the accuracy.

Accuracy \uparrow	UnCal	TS	DirCal	I-Max	Focal	Spline	IOP	GP	MMCE	KCal
IIC (pat)	58.68 \pm 1.42	58.68 \pm 1.42	63.17\pm1.42	57.20 \pm 1.32	54.35 \pm 1.64	58.51 \pm 1.32	58.68 \pm 1.42	58.68 \pm 1.42	58.05 \pm 1.37	61.67\pm2.22
IIC	58.53 \pm 0.06	58.53 \pm 0.06	63.80 \pm 0.10	56.96 \pm 0.14	54.41 \pm 0.05	58.36 \pm 0.20	58.53 \pm 0.06	58.52 \pm 0.06	58.06 \pm 0.04	66.32\pm0.21
ISRUC (pat)	75.11 \pm 0.77	75.11 \pm 0.77	75.57\pm0.91	75.54\pm0.68	73.79 \pm 0.72	75.11 \pm 0.79	75.11 \pm 0.77	75.11 \pm 0.76	76.26\pm0.59	76.13\pm0.89
ISRUC	74.66 \pm 0.08	74.66 \pm 0.08	76.08 \pm 0.16	75.15 \pm 0.07	73.34 \pm 0.09	74.69 \pm 0.09	74.66 \pm 0.08	74.66 \pm 0.09	75.95 \pm 0.07	77.45\pm0.16
PN2017	54.67 \pm 0.14	54.67 \pm 0.14	60.00\pm0.22	57.55 \pm 0.39	13.78 \pm 0.13	55.11 \pm 0.84	55.15 \pm 1.48	54.69 \pm 0.15	51.90 \pm 0.07	60.36\pm0.61
C10 (ViT)	98.94\pm0.05	98.94\pm0.05	98.94\pm0.05	98.94\pm0.05	98.76 \pm 0.06	98.94\pm0.05	98.94\pm0.05	98.94\pm0.06	98.93\pm0.07	98.98\pm0.09
C10 (Mixer)	98.17\pm0.08	98.17\pm0.08	98.03\pm0.09	98.13\pm0.08	96.98 \pm 0.08	98.17\pm0.08	98.17\pm0.08	98.16\pm0.08	98.15\pm0.06	98.14\pm0.06
C100 (ViT)	92.09 \pm 0.16	92.09 \pm 0.16	92.08 \pm 0.14	91.95 \pm 0.17	91.21 \pm 0.12	92.09 \pm 0.16	92.09 \pm 0.16	92.09 \pm 0.16	92.41 \pm 0.17	92.37\pm0.15
C100 (Mixer)	87.53 \pm 0.20	87.53 \pm 0.20	87.24 \pm 0.22	87.10 \pm 0.21	86.49 \pm 0.23	87.53 \pm 0.20	87.53 \pm 0.20	87.51 \pm 0.20	88.13\pm0.25	87.55 \pm 0.16
SVHN (ViT)	95.93 \pm 0.05	95.93 \pm 0.05	95.93 \pm 0.05	95.85 \pm 0.06	95.70 \pm 0.08	95.93 \pm 0.05	95.93 \pm 0.05	95.93 \pm 0.05	96.48\pm0.04	96.42\pm0.05
SVHN (Mixer)	95.85 \pm 0.04	95.85 \pm 0.04	95.98 \pm 0.04	95.85 \pm 0.05	95.24 \pm 0.04	95.85 \pm 0.04	95.85 \pm 0.04	95.85 \pm 0.05	95.58 \pm 0.05	96.10\pm0.04
ImageNet	80.44\pm0.24	80.44\pm0.24	79.55 \pm 0.24	80.34\pm0.28	-	80.22\pm0.27	80.44\pm0.24	80.44\pm0.24	-	79.64 \pm 0.24

Table 3: Class-wise ECE in 10^{-2} (\downarrow means lower=better). The best accuracy-preserving method is in **bold** ($p=0.01$). The lowest but not accuracy-preserving number is underscored. KCal almost always achieves the lowest class-wise ECE, while maintaining accuracy.

CECE \downarrow	UnCal	TS	DirCal	I-Max	Focal	Spline	IOP	GP	MMCE	KCal
IIC (pat)	8.07 \pm 0.27	8.97 \pm 0.85	5.13\pm1.48	9.23 \pm 0.98	8.99 \pm 0.53	8.56 \pm 0.62	8.33 \pm 0.50	7.95 \pm 0.64	7.12 \pm 0.43	4.68\pm1.27
IIC	7.96 \pm 0.02	8.96 \pm 0.52	2.24\pm0.13	8.76 \pm 0.26	8.78 \pm 0.02	8.43 \pm 0.21	8.01 \pm 0.25	7.52 \pm 0.23	6.70 \pm 0.25	2.03\pm0.26
ISRUC (pat)	4.48\pm0.24	4.69\pm0.76	4.18\pm0.90	8.56 \pm 1.00	9.23 \pm 0.21	4.68\pm0.46	4.60\pm0.60	4.64\pm0.43	4.08\pm0.36	3.82\pm1.24
ISRUC	4.49 \pm 0.02	5.17 \pm 0.77	2.71 \pm 0.40	9.22 \pm 0.85	9.05 \pm 0.03	4.73 \pm 0.15	4.67 \pm 0.36	4.67 \pm 0.27	4.10 \pm 0.22	1.90\pm0.28
PN2017	12.17 \pm 0.07	12.31 \pm 0.23	4.30\pm0.47	9.92 \pm 1.16	17.31 \pm 0.09	8.61 \pm 0.73	12.09 \pm 0.34	12.17 \pm 0.07	12.35 \pm 0.39	4.25\pm1.26
C10 (ViT)	3.19 \pm 0.01	0.76 \pm 0.04	0.83 \pm 0.06	0.68\pm0.05	4.82 \pm 0.07	0.90 \pm 0.04	0.81 \pm 0.06	0.74\pm0.06	1.11 \pm 0.27	0.74\pm0.07
C10 (Mixer)	3.11 \pm 0.02	1.45 \pm 0.12	1.23 \pm 0.10	1.24\pm0.17	6.70 \pm 0.03	1.28 \pm 0.09	1.30 \pm 0.07	1.21\pm0.07	1.43 \pm 0.19	1.17\pm0.10
C100 (ViT)	5.90 \pm 0.05	5.27 \pm 0.20	4.64 \pm 0.13	4.96 \pm 0.17	5.53 \pm 0.06	4.41\pm0.14	4.72 \pm 0.12	4.65 \pm 0.16	4.27\pm0.23	4.32\pm0.10
C100 (Mixer)	5.39 \pm 0.04	5.82 \pm 0.17	5.25 \pm 0.14	5.79 \pm 0.24	5.72 \pm 0.05	4.92 \pm 0.18	5.34 \pm 0.23	5.09 \pm 0.15	5.26 \pm 0.19	4.62\pm0.10
SVHN (ViT)	3.37 \pm 0.01	2.31 \pm 0.56	1.22\pm0.06	2.64 \pm 0.20	5.89 \pm 0.03	1.34 \pm 0.05	1.39 \pm 0.06	1.40 \pm 0.05	1.47 \pm 0.11	1.23\pm0.10
SVHN (Mixer)	3.20 \pm 0.01	3.06 \pm 0.61	1.21\pm0.12	2.64 \pm 0.17	5.59 \pm 0.02	1.45 \pm 0.09	1.44 \pm 0.06	1.46 \pm 0.06	1.64 \pm 0.13	1.40 \pm 0.08
ImageNet	2.96 \pm 0.02	3.25 \pm 0.07	5.60 \pm 0.23	2.82 \pm 0.19	-	2.17\pm0.06	2.30 \pm 0.14	2.42 \pm 0.06	-	1.94 \pm 0.04

³PN2017 did not provide patient IDs, so we cannot split by patient.

Table 4: ECE in 10^{-2} (\downarrow means lower=better). The best accuracy-preserving method is in **bold** ($p=0.01$). The lowest but not accuracy-preserving number is underscored. KCal is usually on par or better than the best baseline.

ECE \downarrow	UnCal	TS	DirCal	I-Max	Focal	Spline	IOP	GP	MMCE	KCal
IIC (pat)	9.32 \pm 1.01	5.00\pm2.75	2.92\pm1.59	10.52 \pm 4.05	7.53 \pm 0.55	4.58\pm2.04	4.57\pm2.14	3.86\pm1.63	6.33 \pm 3.28	4.34\pm1.35
IIC	9.28 \pm 0.03	4.45 \pm 1.52	1.39\pm0.19	10.16 \pm 0.81	7.25 \pm 0.05	3.20 \pm 0.64	3.50 \pm 0.41	1.80\pm0.49	4.78 \pm 2.24	2.62 \pm 0.59
ISRUC (pat)	3.59 \pm 0.32	2.73\pm1.53	2.97 \pm 0.97	8.86 \pm 1.39	14.88 \pm 0.43	1.98\pm0.35	2.45\pm1.36	2.00\pm0.53	2.12\pm0.93	2.78\pm1.25
ISRUC	3.46 \pm 0.06	3.82 \pm 1.69	2.27 \pm 0.69	9.58 \pm 1.23	14.70 \pm 0.06	1.50\pm0.53	2.71 \pm 0.96	2.09 \pm 0.74	2.12\pm1.03	1.36\pm0.41
PN2017	16.70 \pm 0.22	16.99 \pm 0.73	5.64\pm0.75	10.40 \pm 1.35	24.63 \pm 0.13	6.84\pm2.09	16.07 \pm 2.03	16.66 \pm 0.21	13.49 \pm 1.07	4.78\pm1.48
C10 (ViT)	9.15 \pm 0.05	0.75 \pm 0.11	0.40 \pm 0.04	0.51 \pm 0.07	7.17 \pm 0.07	0.39 \pm 0.08	0.39 \pm 0.04	0.21\pm0.06	0.42\pm0.29	0.40 \pm 0.05
C10 (Mixer)	9.04 \pm 0.06	1.06 \pm 0.12	0.61 \pm 0.07	0.91 \pm 0.14	12.53 \pm 0.06	0.36\pm0.06	0.66 \pm 0.09	0.34\pm0.10	0.91 \pm 0.44	0.59 \pm 0.09
C100 (ViT)	11.64 \pm 0.14	2.77 \pm 0.46	0.74\pm0.16	3.28 \pm 0.22	9.97 \pm 0.09	1.08 \pm 0.18	1.07 \pm 0.19	0.88\pm0.11	1.05 \pm 0.30	1.50 \pm 0.32
C100 (Mixer)	13.71 \pm 0.15	3.03 \pm 0.34	<u>1.06\pm0.28</u>	4.75 \pm 0.27	14.35 \pm 0.21	1.25\pm0.29	1.70 \pm 0.66	1.08\pm0.26	1.93 \pm 0.49	3.07 \pm 0.49
SVHN (ViT)	10.10 \pm 0.05	2.43\pm2.72	0.60\pm0.07	2.05 \pm 0.18	12.17 \pm 0.08	0.74 \pm 0.10	0.62\pm0.08	0.64\pm0.07	0.72\pm0.21	0.64\pm0.12
SVHN (Mixer)	10.29 \pm 0.04	3.19 \pm 2.55	0.66\pm0.05	2.13 \pm 0.10	11.09 \pm 0.06	0.78 \pm 0.11	0.60\pm0.08	0.72 \pm 0.06	0.72 \pm 0.28	0.73 \pm 0.10
ImageNet	3.21 \pm 0.15	3.52 \pm 0.13	4.30 \pm 0.68	7.97 \pm 0.35	-	1.10 \pm 0.20	1.31 \pm 0.47	0.87\pm0.12	-	1.43 \pm 0.34

Table 5: Brier Score in 10^{-2} (\downarrow means lower=better). The best accuracy-preserving methods are in **bold** ($p=0.01$). The lowest but not accuracy-preserving number is underscored.

Brier \downarrow	UnCal	TS	DirCal	I-Max	Focal	Spline	IOP	GP	MMCE	KCal
IIC (pat)	21.30 \pm 0.25	20.70 \pm 0.69	18.94\pm0.55	21.09 \pm 1.29	21.48 \pm 0.19	20.43 \pm 0.50	20.52 \pm 0.58	20.33 \pm 0.42	21.11 \pm 0.71	19.33\pm0.78
IIC	21.35 \pm 0.01	20.62 \pm 0.27	18.33 \pm 0.04	20.83 \pm 0.19	21.46 \pm 0.01	20.21 \pm 0.09	20.39 \pm 0.09	20.05 \pm 0.08	20.86 \pm 0.26	17.54\pm0.10
ISRUC (pat)	15.26 \pm 0.25	15.20 \pm 0.31	15.37 \pm 0.38	16.25 \pm 0.49	18.55 \pm 0.18	15.11 \pm 0.26	15.16 \pm 0.31	15.16 \pm 0.29	14.69\pm0.22	14.97\pm0.29
ISRUC	15.46 \pm 0.03	15.50 \pm 0.19	15.07 \pm 0.09	16.62 \pm 0.33	18.77 \pm 0.01	15.31 \pm 0.05	15.39 \pm 0.10	15.35 \pm 0.06	14.91 \pm 0.08	14.28\pm0.08
PN2017	26.61 \pm 0.05	26.74 \pm 0.27	22.44\pm0.15	24.58 \pm 0.59	<u>17.79\pm0.03</u>	23.28 \pm 0.37	26.39 \pm 0.69	26.61 \pm 0.05	26.41 \pm 0.44	22.56\pm0.28
C10 (ViT)	1.76 \pm 0.03	0.89 \pm 0.06	0.78\pm0.04	0.84 \pm 0.04	<u>1.75\pm0.03</u>	0.79\pm0.04	0.79\pm0.04	0.78\pm0.04	0.85 \pm 0.10	0.75\pm0.05
C10 (Mixer)	2.29 \pm 0.03	1.48 \pm 0.07	1.42 \pm 0.05	1.46 \pm 0.08	4.16 \pm 0.04	1.39 \pm 0.04	1.40 \pm 0.05	1.37\pm0.04	1.45\pm0.16	1.34\pm0.04
C100 (ViT)	6.94 \pm 0.08	5.35 \pm 0.15	5.17 \pm 0.10	5.48 \pm 0.14	6.93 \pm 0.07	5.19 \pm 0.09	5.18 \pm 0.10	5.14 \pm 0.09	4.81\pm0.10	5.01 \pm 0.08
C100 (Mixer)	10.15 \pm 0.11	7.94 \pm 0.17	7.82 \pm 0.12	8.23 \pm 0.17	10.91 \pm 0.08	7.76 \pm 0.12	7.82 \pm 0.15	7.72 \pm 0.13	7.38\pm0.16	7.61 \pm 0.09
SVHN (ViT)	3.99 \pm 0.03	3.03 \pm 0.34	2.78 \pm 0.04	2.99 \pm 0.07	5.03 \pm 0.03	2.80 \pm 0.03	2.79 \pm 0.04	2.79 \pm 0.04	2.43\pm0.02	2.49 \pm 0.03
SVHN (Mixer)	4.03 \pm 0.03	3.21 \pm 0.36	2.77 \pm 0.03	3.04 \pm 0.04	5.06 \pm 0.04	2.84 \pm 0.03	2.81 \pm 0.04	2.81 \pm 0.04	3.03 \pm 0.02	2.68\pm0.03
ImageNet	11.15 \pm 0.14	11.20 \pm 0.15	12.03 \pm 0.21	11.93 \pm 0.18	-	10.68\pm0.13	10.69\pm0.13	10.67\pm0.12	-	11.14 \pm 0.10

4.2 BASELINES METHODS

We compare KCal with the multiple state-of-the-art calibration methods, including Temperature Scaling (TS) (Guo et al., 2017), Dirichlet Calibration (DirCal) (Kull et al., 2019), Mutual-information-maximization-based Binning (I-Max) (Patel et al., 2021), Gaussian Process Calibration (GP) (Wenger et al., 2020), Intra Order-preserving Calibration (IOP) (Rahimi et al., 2020), Splines-based Calibration (Spline) (Gupta et al., 2021), Focal-loss-based calibration (Focal) (Mukhoti et al., 2020), MMCE-based calibration (MMCE) (Kumar et al., 2018).

4.3 EVALUATION METRICS

We report standard evaluation metrics: Accuracy, class-wise expected calibration error (CECE) (Kull et al., 2019; Patel et al., 2021; Nixon et al., 2019), expected calibration error (ECE) (Guo et al., 2017), and Brier score (Brier, 1950). CECE is typically used as a proxy to evaluate full calibration quality, because directly binning basing on the entire vector $\hat{\mathbf{p}}$ requires exponentially (in K) many bins. Similar to Patel et al. (2021); Nixon et al. (2019), we ignore all predictions with very small probabilities (less than $\max\{0.01, \frac{1}{K}\}$). ECE, on the other hand, only measures confidence calibration (Def 2). For both ECE and CECE, we use the ‘‘adaptive’’ version with equal number of samples in each bin (with 20 bins), because this is shown to measure the calibration quality better than the equal-width version (Nixon et al., 2019). Brier score can be viewed as the sum of a ‘‘calibration’’ term, and a ‘‘refinement’’ term measuring how discriminative a model is (Kull & Flach, 2015). Here we focus on the brier score of the top class. We refer to (Guo et al., 2017; Kull et al., 2019; Nixon et al., 2019) for further discussion on these metrics.

4.4 RESULTS

The results are presented in Tables 2, 3, 4 and 5. All experiments are repeated 10 times by reshuffling calibration and test sets, and the standard deviations are reported. For ImageNet, we skipped Focal and MMCE because the base NN is given and these methods require training from scratch. Due to space constraints, we include ablation studies in the Appendix.

Table 6: Ranks for different evaluation metrics. The best rank is underscored. In general, KCal consistently outperforms baselines on Accuracy, CECE and Brier, and the difference between most methods on ECE is small.

Ranking	UnCal	TS	DirCal	I-Max	Focal	Spline	IOP	GP	MMCE	KCal
ECE	8.42±1.43	6.68±1.11	3.33±1.80	7.73±1.55	9.39±0.95	3.51±1.06	4.25±1.35	2.91±1.66	4.52±0.98	3.84±1.35
Accuracy	5.03±1.30	5.03±1.30	4.53±2.69	6.41±2.36	9.99±0.03	5.56±0.93	5.01±1.27	5.64±1.16	4.74±3.30	<u>2.70±2.01</u>
CECE	6.99±1.95	7.41±1.60	3.31±2.08	6.82±2.67	9.46±0.61	4.59±2.06	5.12±1.13	4.37±1.27	4.69±1.99	<u>1.83±0.76</u>
Brier	8.18±1.52	6.91±0.85	3.86±2.08	7.42±1.06	8.98±2.67	4.23±1.05	4.88±1.24	3.89±1.83	4.11±2.89	<u>2.05±1.17</u>
Average	7.16	6.51	3.76	7.09	9.46	4.47	4.81	4.20	4.51	<u>2.61</u>

In general, KCal has the best CECE, accuracy and Brier score, and is highly competitive in terms of ECE as well. Note that KCal is also the only method with provable calibration guarantee. TS is effective in controlling overall ECE but shows little improvement on CECE over UnCal. DirCal often ranks high for the calibration quality but tends to decrease accuracy as K increases. DirCal’s performance also has a higher cost: Every experiment requires training over hundreds of models with SGD and taking the best ensemble, accounting for most of the experiment computation cost in this paper. The amount of tuning suggested for good performance indicates sensitivity to the choice of hyper-parameters, which we have indeed observed to be the case. Spline, IOP and GP are similar to DirCal on vision datasets, but generally perform worse on the healthcare datasets. In Patel et al. (2021), I-Max lowers ECE and CECE significantly. However, it has a critical issue - it does *not* produce a valid probability vector⁴. Once normalized, as reported in our experiments, the performance worsens. Since calibrating all the classes simultaneously is *the* distinguishing challenge in multiclass classification, we interpret the observation as: If this normalization constraint is removed, the “optimization problem” (to lower calibration error) is much simpler, but the results are invalid hence unusable probability vectors. Spline also requires a re-normalization step, but its performance stays consistent. Focal is worse than the UnCal in many experiments. While calibration performance may improve by combing Focal with other methods, the drop in accuracy is harder to overcome⁵. We also observed that for healthcare datasets, being able to tune on a different set of patients boosts the performance significantly. This is reflected in the accuracy gain for DirCal and KCal, and suggests that the embeddings/logits are quite transferable, but the prediction criteria itself can vary from patient to patient.

Finally, we summarize the rankings of all datasets in Table 6. It is clear that KCal consistently improves calibration quality for all classes and maintains or improves accuracy. And if we look at only the confidence prediction (Brier or ECE), KCal is still highly competitive.

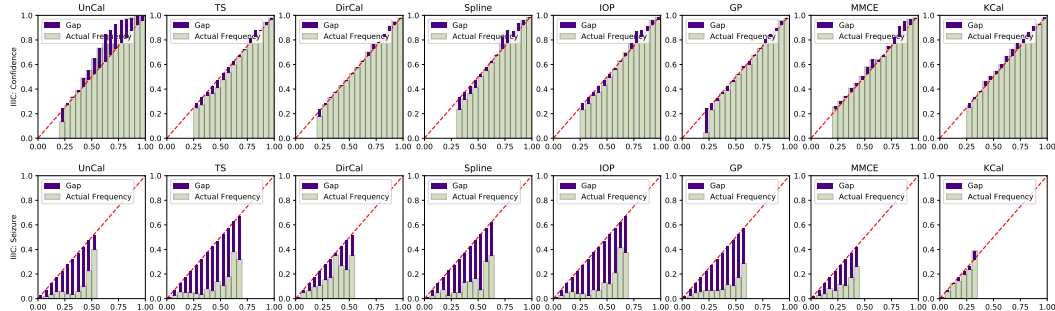


Figure 2: Reliability diagrams for the predicted class (top) and Seizure (bottom) in IIC. All methods calibrate confidence well, but only KCal achieves reasonable calibration quality for Seizure.

4.5 CASE STUDY FOR SEIZURE PREDICTION

We show the reliability diagrams (Kull et al., 2019; Guo et al., 2017) on the IIC dataset to illustrate the importance of full calibration in Figure 2. We include both the the predicted class (confidence calibration) and Seizure. More reliability diagrams can be found in the Appendix, and the results

⁴It generates a vector whose sum ranges from 0.4 to 2.0 in our experiments. The range is wider for a larger K .

⁵In PN2017, rare classes are oversampled during training (Hong et al., 2019). While this did not cause issues for other calibration methods, the distributional shift at test time seems catastrophic for Focal.

are consistent for all classes. The un-calibrated predictions have large gaps for both confidence and Seizure. Most baselines provide calibrated confidence calibration, but fail to calibrated the output for the rare class Seizure. KCal, on the other hand, achieves the most consistent results. We note again that since all competing classes must be considered together for any clinical decision, *full* calibration is indispensable in medical applications.

5 CONCLUSION

This paper proposed KCal, a learned-kernel-based calibration method for deep learning models. KCal consists of a supervised dimensionality reduction step on the penultimate layer neural network embedding to improve efficiency. A KDE classifier using the calibration set is employed in this new metric space. As a natural consequence of the construction, KCal provides a calibrated probability vector prediction for all classes. Unlike most existing calibration methods, KCal is also *provably* asymptotically *fully* calibrated with finite sample error bounds. We also showed that empirically, it outperforms existing state-of-the-art calibration methods in terms of accuracy and calibration quality. Moreover, KCal is more robust to distributional shift, which is common in high-risk applications such as healthcare, where calibration is far more crucial. The major limitation of KCal is the need to store the entire calibration set, which is a small overhead with the dimension reduction step and potential improvements.

REFERENCES

- Siddharth Biswal, Joshua A. Kulas, Haoqi Sun, Balaji Goparaju, Michael Brandon Westover, Matt T. Bianchi, and Jimeng Sun. Sleepnet: Automated sleep staging system via deep learning. *ArXiv*, abs/1707.08262, 2017.
- Glenn W. Brier. Verification of Forecasts Expressed in Terms of Probability. *Monthly Weather Review*, 78(1):1, January 1950. doi: 10.1175/1520-0493(1950)078<0001:VOFEIT>2.0.CO;2.
- José E. Chacón and Tarn Duong. *Multivariate Kernel Smoothing and its Applications*. Chapman and Hall, 2018.
- Yutian Chen, Max Welling, and Alex Smola. Super-samples from kernel herding. In *Proceedings of the Twenty-Sixth Conference on Uncertainty in Artificial Intelligence*, UAI’10, pp. 109–116, Arlington, Virginia, USA, 2010. AUAI Press. ISBN 9780974903965.
- Gari D. Clifford, Chengyu Liu, Benjamin Moody, Liwei H. Lehman, Ikaro Silva, Qiao Li, A. E. Johnson, and Roger G. Mark. AF classification from a short single lead ECG recording: The PhysioNet/computing in cardiology challenge 2017. In *Computing in Cardiology*, 2017. doi: 10.22489/CinC.2017.065-469.
- Morris H. Degroot and Stephen E. Fienberg. The comparison and evaluation of forecasters. *The Statistician*, 32:12–22, 1983.
- Jia Deng, Wei Dong, Richard Socher, Li-Jia Li, Kai Li, and Li Fei-Fei. Imagenet: A large-scale hierarchical image database. In *2009 IEEE Conference on Computer Vision and Pattern Recognition*, pp. 248–255, 2009. doi: 10.1109/CVPR.2009.5206848.
- Li Deng, Geoffrey Hinton, and Brian Kingsbury. New types of deep neural network learning for speech recognition and related applications: an overview. In *2013 IEEE International Conference on Acoustics, Speech and Signal Processing*, pp. 8599–8603, 2013. doi: 10.1109/ICASSP.2013.6639344.
- Alexey Dosovitskiy, Lucas Beyer, Alexander Kolesnikov, Dirk Weissenborn, Xiaohua Zhai, Thomas Unterthiner, Mostafa Dehghani, Matthias Minderer, Georg Heigold, Sylvain Gelly, Jakob Uszkoreit, and Neil Houlsby. An image is worth 16x16 words: Transformers for image recognition at scale. In *International Conference on Learning Representations*, 2021. URL <https://openreview.net/forum?id=YicbFdNTTy>.

- ATelmo Silva Filho, Hao Song, Miquel Perello-Nieto, Raul Santos-Rodriguez, Meelis Kull, and Peter Flach. Classifier calibration: How to assess and improve predicted class probabilities: a survey. *CoRR*, abs/2112.10327, 2021. URL <https://arxiv.org/abs/2112.10327>.
- Sébastien Gadat, Thierry Klein, and Clément Marteau. Classification in general finite dimensional spaces with the k-nearest neighbor rule. *The Annals of Statistics*, 44(3):982–1009, 2016. ISSN 00905364. URL <http://www.jstor.org/stable/43818918>.
- Wendong Ge, Jin Jing, Sungtae An, Aline Herlopian, Marcus Ng, Aaron F. Struck, Brian Ap-pavu, Emily L. Johnson, Gamaleldin Osman, Hiba A. Haider, Ioannis Karakis, Jennifer A. Kim, Jonathan J. Halford, Monica B. Dhakar, Rani A. Sarkis, Christa B. Swisher, Sarah Schmitt, Jong Woo Lee, Mohammad Tabaeizadeh, Andres Rodriguez, Nicolas Gaspard, Emily Gilmore, Susan T. Herman, Peter W. Kaplan, Jay Pathmanathan, Shenda Hong, Eric S. Rosenthal, Sahar Zafar, Jimeng Sun, and M. Brandon Westover. Deep active learning for interictal ictal injury continuum EEG patterns. *Journal of Neuroscience Methods*, 351:108966, mar 2021. doi: 10.1016/j.jneumeth.2020.108966. URL <https://doi.org/10.1016%2Fj.jneumeth.2020.108966>.
- A. L. Goldberger, L. A. Amaral, L. Glass, J. M. Hausdorff, P. C. Ivanov, R. G. Mark, J. E. Mietus, G. B. Moody, C. K. Peng, and H. E. Stanley. PhysioBank, PhysioToolkit, and PhysioNet: components of a new research resource for complex physiologic signals. *Circulation*, 2000. ISSN 15244539. doi: 10.1161/01.cir.101.23.e215.
- Alexander G. Gray and Andrew W. Moore. Nonparametric density estimation: Toward computational tractability. In *SDM*, 2003.
- Chuan Guo, Geoff Pleiss, Yu Sun, and Kilian Q. Weinberger. On calibration of modern neural networks. In Doina Precup and Yee Whye Teh (eds.), *Proceedings of the 34th International Conference on Machine Learning*, volume 70 of *Proceedings of Machine Learning Research*, pp. 1321–1330. PMLR, 06–11 Aug 2017. URL <https://proceedings.mlr.press/v70/guo17a.html>.
- Chirag Gupta and Aaditya Ramdas. Distribution-free calibration guarantees for histogram binning without sample splitting. In Marina Meila and Tong Zhang (eds.), *Proceedings of the 38th International Conference on Machine Learning*, volume 139 of *Proceedings of Machine Learning Research*, pp. 3942–3952. PMLR, 18–24 Jul 2021. URL <https://proceedings.mlr.press/v139/gupta21b.html>.
- Kartik Gupta, Amir Rahimi, Thalaiyasingam Ajanthan, Thomas Mensink, Cristian Sminchisescu, and Richard Hartley. Calibration of neural networks using splines. In *International Conference on Learning Representations*, 2021. URL <https://openreview.net/forum?id=eQe8DEWNN2W>.
- Shenda Hong, Cao Xiao, Tengfei Ma, Hongyan Li, and Jimeng Sun. Mina: Multilevel knowledge-guided attention for modeling electrocardiography signals. In *IJCAI International Joint Conference on Artificial Intelligence*, 2019. ISBN 9780999241141. doi: 10.24963/ijcai.2019/816.
- Heinrich Jiang. Uniform convergence rates for kernel density estimation. In Doina Precup and Yee Whye Teh (eds.), *Proceedings of the 34th International Conference on Machine Learning*, volume 70 of *Proceedings of Machine Learning Research*, pp. 1694–1703. PMLR, 06–11 Aug 2017. URL <https://proceedings.mlr.press/v70/jiang17b.html>.
- Heinrich Jiang, Been Kim, Melody Guan, and Maya Gupta. To trust or not to trust a classifier. In S. Bengio, H. Wallach, H. Larochelle, K. Grauman, N. Cesa-Bianchi, and R. Garnett (eds.), *Advances in Neural Information Processing Systems*, volume 31. Curran Associates, Inc., 2018. URL <https://proceedings.neurips.cc/paper/2018/file/7180cfff6a8e829dacfc2a31b3f72ece-Paper.pdf>.
- Xiaoqian Jiang, Melanie Osl, Jihoon Kim, and Lucila Ohno-Machado. Calibrating predictive model estimates to support personalized medicine. *J. Am. Medical Informatics Assoc.*, 19(2): 263–274, 2012. doi: 10.1136/amiajnl-2011-000291. URL <https://doi.org/10.1136/amiajnl-2011-000291>.

- Jin Jing, Emile d'Angremont, Senan Ebrahim, Mohammad Tabaeizadeh, Marcus Ng, Aline Herlopian, Justin Dauwels, and M. Brandon Westover. Rapid annotation of seizures and interictal-ictal-injury continuum eeg patterns. *Journal of Neuroscience Methods*, 347:108956, 2021. ISSN 0165-0270. doi: <https://doi.org/10.1016/j.jneumeth.2020.108956>. URL <https://www.sciencedirect.com/science/article/pii/S0165027020303794>.
- Archit Karandikar, Nicholas Cain, Dustin Tran, Balaji Lakshminarayanan, Jonathon Shlens, Michael C. Mozer, and Becca Roelofs. Soft calibration objectives for neural networks. *CoRR*, abs/2108.00106, 2021. URL <https://arxiv.org/abs/2108.00106>.
- Sirvan Khalighi, Teresa Sousa, José Moutinho Santos, and Urbano Nunes. ISRUC-Sleep: A comprehensive public dataset for sleep researchers. *Computer Methods and Programs in Biomedicine*, 2016. ISSN 18727565. doi: 10.1016/j.cmpb.2015.10.013.
- J. Kiefer. Sequential minimax search for a maximum. *Proceedings of the American Mathematical Society*, 4(3):502–506, 1953. ISSN 00029939, 10886826. URL <http://www.jstor.org/stable/2032161>.
- Alex Krizhevsky. Learning multiple layers of features from tiny images, 2009.
- Meelis Kull and Peter Flach. Novel decompositions of proper scoring rules for classification: Score adjustment as precursor to calibration. In Annalisa Appice, Pedro Pereira Rodrigues, Vitor Santos Costa, Carlos Soares, João Gama, and Alípio Jorge (eds.), *Machine Learning and Knowledge Discovery in Databases*, pp. 68–85, Cham, 2015. Springer International Publishing. ISBN 978-3-319-23528-8.
- Meelis Kull, Miquel Perello Nieto, Markus Kängsepp, Telmo Silva Filho, Hao Song, and Peter Flach. Beyond temperature scaling: Obtaining well-calibrated multi-class probabilities with dirichlet calibration. In *Advances in Neural Information Processing Systems*, pp. 12295–12305, 2019.
- Ananya Kumar, Percy S Liang, and Tengyu Ma. Verified uncertainty calibration. In H. Wallach, H. Larochelle, A. Beygelzimer, F. d'Alché-Buc, E. Fox, and R. Garnett (eds.), *Advances in Neural Information Processing Systems*, volume 32. Curran Associates, Inc., 2019. URL <https://proceedings.neurips.cc/paper/2019/file/f8c0c968632845cd133308b1a494967f-Paper.pdf>.
- Aviral Kumar, Sunita Sarawagi, and Ujjwal Jain. Trainable calibration measures for neural networks from kernel mean embeddings. In Jennifer Dy and Andreas Krause (eds.), *Proceedings of the 35th International Conference on Machine Learning*, volume 80 of *Proceedings of Machine Learning Research*, pp. 2805–2814. PMLR, 10–15 Jul 2018. URL <https://proceedings.mlr.press/v80/kumar18a.html>.
- Xingchen Ma and Matthew B. Blaschko. Meta-cal: Well-controlled post-hoc calibration by ranking. In Marina Meila and Tong Zhang (eds.), *Proceedings of the 38th International Conference on Machine Learning*, volume 139 of *Proceedings of Machine Learning Research*, pp. 7235–7245. PMLR, 18–24 Jul 2021. URL <https://proceedings.mlr.press/v139/ma21a.html>.
- Jishnu Mukhoti, Viveka Kulharia, Amartya Sanyal, Stuart Golodetz, Philip Torr, and Puneet Dokania. Calibrating deep neural networks using focal loss. In H. Larochelle, M. Ranzato, R. Hadsell, M. F. Balcan, and H. Lin (eds.), *Advances in Neural Information Processing Systems*, volume 33, pp. 15288–15299. Curran Associates, Inc., 2020. URL <https://proceedings.neurips.cc/paper/2020/file/aeb7b30ef1d024a76f21a1d40e30c302-Paper.pdf>.
- Allan H. Murphy and Robert L. Winkler. Reliability of subjective probability forecasts of precipitation and temperature. *Journal of The Royal Statistical Society Series C-applied Statistics*, 26:41–47, 1977.
- Allan H. Murphy and Robert L. Winkler. Probability forecasting in meteorology. *Journal of the American Statistical Association*, 79:489–500, 1984.
- Yuval Netzer, Tao Wang, Adam Coates, Alessandro Bissacco, Bo Wu, and Andrew Y. Ng. Reading digits in natural images with unsupervised feature learning. In *NIPS Workshop on Deep Learning and Unsupervised Feature Learning 2011*, 2011. URL http://ufldl.stanford.edu/housenumbers/nips2011_housenumbers.pdf.

- Alexandru Niculescu-Mizil and Rich Caruana. Predicting good probabilities with supervised learning. In *Proceedings of the 22nd International Conference on Machine Learning, ICML '05*, pp. 625–632, New York, NY, USA, 2005. Association for Computing Machinery. ISBN 1595931805. doi: 10.1145/1102351.1102430. URL <https://doi.org/10.1145/1102351.1102430>.
- Jeremy Nixon, Michael W. Dusenberry, Linchuan Zhang, Ghassen Jerfel, and Dustin Tran. Measuring calibration in deep learning. In *Proceedings of the IEEE/CVF Conference on Computer Vision and Pattern Recognition (CVPR) Workshops*, June 2019.
- Wanli Ouyang and Xiaogang Wang. Joint deep learning for pedestrian detection. In *Proceedings of the IEEE International Conference on Computer Vision (ICCV)*, December 2013.
- Nicolas Papernot and Patrick D. McDaniel. Deep k-nearest neighbors: Towards confident, interpretable and robust deep learning. *CoRR*, abs/1803.04765, 2018. URL <http://arxiv.org/abs/1803.04765>.
- Kanil Patel, William H. Beluch, Bin Yang, Michael Pfeiffer, and Dan Zhang. Multi-class uncertainty calibration via mutual information maximization-based binning. In *International Conference on Learning Representations*, 2021. URL <https://openreview.net/forum?id=AICNpd8ke-m>.
- John C. Platt. Probabilistic outputs for support vector machines and comparisons to regularized likelihood methods. In *ADVANCES IN LARGE MARGIN CLASSIFIERS*, pp. 61–74. MIT Press, 1999.
- Zhi Qiao, Austin Bae, Lucas M Glass, Cao Xiao, and Jimeng Sun. FLANNEL (Focal Loss bAsed Neural Network EnsemblE) for COVID-19 detection. *Journal of the American Medical Informatics Association*, 28(3):444–452, 10 2020. ISSN 1527-974X. doi: 10.1093/jamia/ocaa280. URL <https://doi.org/10.1093/jamia/ocaa280>.
- Amir Rahimi, Amirreza Shaban, Ching-An Cheng, Richard Hartley, and Byron Boots. Intra order-preserving functions for calibration of multi-class neural networks. In H. Larochelle, M. Ranzato, R. Hadsell, M.F. Balcan, and H. Lin (eds.), *Advances in Neural Information Processing Systems*, volume 33, pp. 13456–13467. Curran Associates, Inc., 2020. URL <https://proceedings.neurips.cc/paper/2020/file/9bc99c590be3511b8d53741684ef574c-Paper.pdf>.
- Giulio Ruffini, David Ibañez, Marta Castellano, Laura Dubreuil-Vall, Aureli Soria-Frisch, Ron Postuma, Jean-François Gagnon, and Jacques Montplaisir. Deep learning with eeg spectrograms in rapid eye movement behavior disorder. *Frontiers in Neurology*, 10, 2019. ISSN 1664-2295. doi: 10.3389/fneur.2019.00806. URL <https://www.frontiersin.org/article/10.3389/fneur.2019.00806>.
- Danaipat Sodkomkham, Davide Ciliberti, Matthew A. Wilson, Ken ichi Fukui, Koichi Moriyama, Masayuki Numao, and Fabian Kloosterman. Kernel density compression for real-time bayesian encoding/decoding of unsorted hippocampal spikes. *Knowledge-Based Systems*, 94:1–12, 2016. ISSN 0950-7051. doi: <https://doi.org/10.1016/j.knosys.2015.09.013>. URL <https://www.sciencedirect.com/science/article/pii/S0950705115003524>.
- Christian Szegedy, Sergey Ioffe, Vincent Vanhoucke, and Alexander A. Alemi. Inception-v4, inception-resnet and the impact of residual connections on learning. In *Proceedings of the Thirty-First AAAI Conference on Artificial Intelligence, AAAI'17*, pp. 4278–4284. AAAI Press, 2017.
- Ilya O. Tolstikhin, Neil Houlsby, Alexander Kolesnikov, Lucas Beyer, Xiaohua Zhai, Thomas Unterthiner, Jessica Yung, Andreas Steiner, Daniel Keysers, Jakob Uszkoreit, Mario Lucic, and Alexey Dosovitskiy. Mlp-mixer: An all-mlp architecture for vision. *CoRR*, abs/2105.01601, 2021. URL <https://arxiv.org/abs/2105.01601>.
- Juozas Vaicenavicius, David Widmann, Carl Andersson, Fredrik Lindsten, Jacob Roll, and Thomas Schön. Evaluating model calibration in classification. In Kamalika Chaudhuri and Masashi Sugiyama (eds.), *Proceedings of the Twenty-Second International Conference on Artificial*

- Intelligence and Statistics*, volume 89 of *Proceedings of Machine Learning Research*, pp. 3459–3467. PMLR, 16–18 Apr 2019. URL <https://proceedings.mlr.press/v89/vaicenavicius19a.html>.
- Jonathan Wenger, Hedvig Kjellström, and Rudolph Triebel). Non-parametric calibration for classification. In Silvia Chiappa and Roberto Calandra (eds.), *Proceedings of the Twenty Third International Conference on Artificial Intelligence and Statistics*, volume 108 of *Proceedings of Machine Learning Research*, pp. 178–190. PMLR, 26–28 Aug 2020. URL <https://proceedings.mlr.press/v108/wenger20a.html>.
- David Widmann, Fredrik Lindsten, and Dave Zachariah. Calibration tests in multi-class classification: A unifying framework. In H. Wallach, H. Larochelle, A. Beygelzimer, F. d'Alché-Buc, E. Fox, and R. Garnett (eds.), *Advances in Neural Information Processing Systems*, volume 32. Curran Associates, Inc., 2019. URL <https://proceedings.neurips.cc/paper/2019/file/1c336b8080f82bcc2cd2499b4c57261d-Paper.pdf>.
- Ross Wightman. Pytorch image models. <https://github.com/rwightman/pytorch-image-models>, 2019.
- Ye Yuan, Guangxu Xun, Kebin Jia, and Aidong Zhang. A multi-view deep learning framework for eeg seizure detection. *IEEE Journal of Biomedical and Health Informatics*, 23(1):83–94, 2019. doi: 10.1109/JBHI.2018.2871678.
- Bianca Zadrozny and Charles Elkan. Learning and making decisions when costs and probabilities are both unknown. In *Proceedings of the Seventh ACM SIGKDD International Conference on Knowledge Discovery and Data Mining*, KDD '01, pp. 204–213, New York, NY, USA, 2001. Association for Computing Machinery. ISBN 158113391X. doi: 10.1145/502512.502540. URL <https://doi.org/10.1145/502512.502540>.
- Bianca Zadrozny and Charles Elkan. Transforming classifier scores into accurate multiclass probability estimates. In *Proceedings of the Eighth ACM SIGKDD International Conference on Knowledge Discovery and Data Mining*, KDD '02, pp. 694–699, New York, NY, USA, 2002. Association for Computing Machinery. ISBN 158113567X. doi: 10.1145/775047.775151. URL <https://doi.org/10.1145/775047.775151>.
- Jize Zhang, Bhavya Kailkhura, and T. Yong-Jin Han. Mix-n-match : Ensemble and compositional methods for uncertainty calibration in deep learning. In Hal Daumé III and Aarti Singh (eds.), *Proceedings of the 37th International Conference on Machine Learning*, volume 119 of *Proceedings of Machine Learning Research*, pp. 11117–11128. PMLR, 13–18 Jul 2020. URL <https://proceedings.mlr.press/v119/zhang20k.html>.

Appendix

Overview of Appendices: Appendix A contains proofs for the lemmata and theorems that appear in Section 3.3. Appendix B clarifies the benefits of the sampling method (equal-size stratified sampling) described in Section 3.4. Appendix C contains more details on the experiments in this paper. Appendix D compares KCal with a simpler variant, namely KCal-Linear, which uses a linear layer as the Π . Appendix F explores the effect of d , the projected dimension, on the performance and computational overhead. Finally, Appendix G compares the cross-validation-selected bandwidth vs the analytically computed bandwidth, which shows that it is possible to avoid most of the bandwidth selection steps if we use KCal in an online manner.

A DETAILED ASSUMPTIONS AND PROOFS

A.1 ASSUMPTIONS AND DEFINITIONS

Denote $Z_i := \Pi(\mathbf{f}(X_i))$ for $i \in [N + 1]$. We assume $\{Z_i\}_{i=1}^{N+1}$ are i.i.d. Since fixing Π and \mathbf{f} using S_{train} , all data will now live in $\mathcal{Z} := \Pi(\mathbf{f}(\mathcal{X}))$. We are just performing a standard (multivariate) kernel density estimation with only one parameter b on the calibration set. We will use \hat{g} and g to denote the estimation and density in \mathcal{Z} , instead of the more cumbersome $\hat{f}_{\Pi \circ \mathbf{f}, k}$ and $f_{\Pi \circ \mathbf{f}, k}$.

Like in Chacón & Duong (2018), we make the following standard assumptions for $g_k(\mathcal{Z})$:

- (For any k) g_k is square integrable and twice differentiable, with all second order partials bounded, continuous and square integrable.

The base “mother kernel” function should satisfy the following (true for the RBF kernel):

- ϕ is spherical symmetric and has a finite second moment. Formally, this means $\int_{\mathbb{R}^d} x\phi(x)dx = \mathbf{0}$ and $\forall i \in [d], \int_{\mathbb{R}^d} x_i x_j \phi(x)dx = \mu_{2, \phi} \mathbf{1}\{i = j\}$ where $\mu_{2, \phi}$ is a fixed finite constant.

In the proof for Lemma 3.1 and Lemma 3.2, for simplicity, we ignore the subscript k and write g instead of g_k where there is no confusion.

A.2 PROOF OF LEMMA 3.1

Rewriting Eq. (8), we want to show $\|\hat{g}(\mathbf{z}) - g(\mathbf{z})\|_2$ converges to 0 in probability with an admissible $b(m)$, as $m \rightarrow \infty$. We first derive the expression of the bias and variance of \hat{g} . For the bias, we have:

$$\mathbb{E}[\hat{g}(\mathbf{z})] - g(\mathbf{z}) = \frac{1}{b^d} \mathbb{E} \left[\phi \left(\frac{\mathbf{z} - Z}{b} \right) \right] - g(\mathbf{z}) \quad (13)$$

$$= \frac{1}{b^d} \int \phi \left(\frac{\mathbf{z}' - \mathbf{z}}{b} \right) g(\mathbf{z}') d\mathbf{z}' - g(\mathbf{z}) \quad (14)$$

$$= \int \phi(\mathbf{u}) g(\mathbf{z} + b\mathbf{u}) d\mathbf{u} - g(\mathbf{z}) \quad (15)$$

$$= \int \phi(\mathbf{u}) \left(g(\mathbf{z}) + b(D_g(\mathbf{z}))^\top \mathbf{u} + \frac{1}{2} b^2 \mathbf{u}^\top H_g(\mathbf{z}) \mathbf{u} + o(\|\mathbf{b}\mathbf{u}\|^2) \right) d\mathbf{u} - g(\mathbf{z}) \quad (16)$$

$$= \int \phi(\mathbf{u}) \frac{1}{2} b^2 \mathbf{u}^\top H_g(\mathbf{z}) \mathbf{u} d\mathbf{u} + o(\|\mathbf{b}\mathbf{u}\|^2) \quad (17)$$

$$= \int \phi(\mathbf{u}) \frac{1}{2} b^2 \sum_{i,j} u_i u_j H_{g,i,j}(\mathbf{z}) d\mathbf{u} + o(b^2) \quad (18)$$

$$= \sum_i H_{g,i,i}(\mathbf{z}) \mu_{2,\phi} \frac{b^2}{2} + o(b^2) \quad (19)$$

$$= \frac{b^2}{2} \mu_{2,\phi} \text{tr}(H_g(\mathbf{z})) + o(b^2) \quad (20)$$

$$\implies |\mathbb{E}[\hat{g}(\mathbf{z})] - g(\mathbf{z})| \leq C_{\phi,b} b^2 \quad (21)$$

for some constant $C_{\phi,b}$.

For the variance,

$$\text{Var}(\hat{g}(z)) = \text{Var} \left(\frac{1}{mb^d} \sum_{i=1}^m \phi \left(\frac{\mathbf{z} - Z_i}{b} \right) \right) = \frac{1}{mb^{2d}} \text{Var} \left(\phi \left(\frac{\mathbf{z} - Z}{b} \right) \right) \quad (22)$$

$$\leq \frac{1}{mb^{2d}} \mathbb{E} \left[\phi^2 \left(\frac{\mathbf{z} - Z}{b} \right) \right] = \frac{1}{mb^{2d}} \int \phi^2 \left(\frac{\mathbf{z} - \mathbf{z}'}{b} \right) g(\mathbf{z}') d\mathbf{z}' \quad (23)$$

$$= \frac{1}{mb^d} \int \phi^2(\mathbf{u}) g(\mathbf{z} + b\mathbf{u}) d\mathbf{u} \quad (24)$$

$$= \frac{1}{mb^d} \int \phi^2(\mathbf{u}) \left(g(\mathbf{z}) + b(D_g(\mathbf{z}))^\top \mathbf{u} + o(\|\mathbf{b}\mathbf{u}\|^1) \right) d\mathbf{u} \quad (25)$$

$$= \frac{1}{mb^d} \int \phi^2(\mathbf{u}) g(\mathbf{z}) d\mathbf{u} + o\left(\frac{1}{mb^d}\right) \quad (26)$$

$$= \frac{1}{mb^d} g(\mathbf{z}) \int \phi^2(\mathbf{u}) d\mathbf{u} + o\left(\frac{1}{mb^d}\right) \leq C_{\phi,v} \frac{1}{mb^d}. \quad (27)$$

for some constant $C_{\phi,v}$.

As a result, for any $\mathbf{z} \in \mathcal{Z}$, we have the MSE as:

$$\mathbb{E}[\|\hat{g}(\mathbf{z}) - g(\mathbf{z})\|^2] = \mathbb{E}[\|\hat{g}(\mathbf{z}) - \mathbb{E}[\hat{g}(\mathbf{z})] + \mathbb{E}[\hat{g}(\mathbf{z})] - g(\mathbf{z})\|^2] \quad (28)$$

$$= \mathbb{E}[\|\hat{g}(\mathbf{z}) - \mathbb{E}[\hat{g}(\mathbf{z})]\|^2] + \mathbb{E}[\|\mathbb{E}[\hat{g}(\mathbf{z})] - g(\mathbf{z})\|^2] \quad (29)$$

$$= \underbrace{\text{Var}(\hat{g}(\mathbf{z}))}_{\text{variance}} + \underbrace{(\mathbb{E}[\hat{g}(\mathbf{z})] - g(\mathbf{z}))^2}_{\text{bias}^2} \quad (30)$$

$$\leq C_{\phi,v} \frac{1}{mb^d} + C_{\phi,b} b^4. \quad (31)$$

This means the MSE goes to 0 as long as $b^d m \rightarrow \infty$ and $b \rightarrow 0$. As $m \rightarrow \infty$, we have $\lim_{m \rightarrow \infty} \mathbb{E}[\|\hat{g}(\mathbf{z}) - g(\mathbf{z})\|^2] = 0$.

Now, note that $\hat{g}(\mathbf{z}) = \frac{1}{m} \sum_{j=1}^m V_j$ where $V_j = \frac{1}{b^d} \phi(\frac{\mathbf{z} - \mathbf{Z}_j}{b})$. By Bernstein's inequality, we have

$$\mathbf{P}\{|\hat{g}(\mathbf{z}) - \mathbb{E}[\hat{g}(\mathbf{z})]| > \epsilon\} \leq 2e^{-\frac{(m\epsilon^2)/2}{mC_{\phi,v}b^{-d} + \frac{1}{3}m\epsilon\phi(0)b^{-d}}} \leq e^{-Bmb^d\epsilon^2} \quad (32)$$

for some constant B as long as ϵ is smaller than a constant (say 1). With triangular inequality, we have

$$\mathbf{P}\{|\hat{g}(\mathbf{z}) - g(\mathbf{z})| > \epsilon + C_{\phi,b}b^2\} \leq \mathbf{P}\{|\hat{g}(\mathbf{z}) - \mathbb{E}[\hat{g}(\mathbf{z})]| > \epsilon\} \leq e^{-Bmb^d\epsilon^2} \quad (33)$$

which gives us the conclusion as the RHS goes to 0 as $m \rightarrow \infty$.

A.3 PROOF OF LEMMA 3.2

Lemma 3.2 says that $b = \Theta(m^{-\frac{1}{d+4}})$ is the optimal shrinkage rate to minimize $\mathbb{E}[\|\hat{g}(\mathbf{z}) - g(\mathbf{z})\|^2]$. Following Eq. (31), by letting $C_{\phi,b} \frac{1}{mb^d} = C_{\phi,v}b^4$, we get $b = \Theta(m^{-\frac{1}{d+4}})$. We can also derive this formula by taking the derivative of Eq. (31) with respect to b and setting it to 0, which gives us (asymptotically):

$$\frac{-dC_{\phi,b}}{m}b^{-(d+1)} + 4C_{\phi,v}b^3 = 0 \Rightarrow b^* = C'm^{-\frac{1}{d+4}} \quad (34)$$

for some constant C' . The optimal MSE is thus $O(m^{-\frac{4}{d+4}})$.

A.4 PROOF OF THEOREM 3.3

Denote $m := \min_k \{m_k\}$. $\forall k \in [K]$, Bernstein's inequality⁶ gives us:

$$\mathbb{P}\{|\hat{\pi}_k - \pi_k| \geq \epsilon_1\} \leq 2e^{-\frac{N\epsilon_1^2}{2v_{min} + \frac{2}{3}\epsilon_1}} \leq e^{-B_2N\epsilon_1^2} \quad (36)$$

where $v_{min} = \min_k \{\pi_k(1 - \pi_k)\}$ and some constant B_2 (we find the smallest such constant among all classes), as long as ϵ_1 is smaller than a constant (e.g. 1).

From Eq. 33, with $b = C'm^{\frac{-1}{d+4}}$, and let $\epsilon = m^{\frac{-\lambda}{d+4}}$ for $\lambda \in (0, 2)$, we have, for some constants C_1, B_1 :

$$\mathbb{P}\{|\hat{g}(\mathbf{z}) - g(\mathbf{z})| > C_1m^{\frac{-\lambda}{d+4}}\} \leq e^{-B_1m^{\frac{4-2\lambda}{d+4}}}. \quad (37)$$

Define $\delta_k := e^{-B_1m_k^{\frac{4-2\lambda}{d+4}}} + e^{-B_2N\epsilon_1^2} \leq e^{-B_1m^{\frac{4-2\lambda}{d+4}}} + e^{-B_2N\epsilon_1^2}$. With probability $\geq 1 - \sum_k \delta_k$ (union bound), for all k :

$$|\hat{g}_k(\mathbf{z})\hat{\pi}_k - g_k(\mathbf{z})\pi_k| \leq |\hat{g}_k(\mathbf{z})\hat{\pi}_k - g_k(\mathbf{z})\hat{\pi}_k| + |g_k(\mathbf{z})\hat{\pi}_k - g_k(\mathbf{z})\pi_k| \quad (38)$$

$$\leq C_1m_k^{\frac{-\lambda}{d+4}} + g_k(\mathbf{z})\epsilon_1. \quad (39)$$

⁶One could apply Bennett's inequality to get:

$$\mathbb{P}\{|\hat{\pi}_k - \pi_k| \geq \epsilon_1\} \leq e^{-N\frac{\pi_k}{1-\pi_k}h(\frac{\epsilon_1}{\pi_k})} + e^{-N\frac{1-\pi_k}{\pi_k}h(\frac{\epsilon_1}{1-\pi_k})} \quad (35)$$

and repeat the following proof for a slightly tighter bound. However, the notation is much more complicated.

Denote $g^+(\mathbf{z}) = \max_k g_k(\mathbf{z})$, $g^-(\mathbf{z}) = \min_k g_k(\mathbf{z})$, and $\bar{g}(\mathbf{z}) = \sum_k g_k(\mathbf{z})\pi_k$. Denote $\epsilon_{k,2} := C_1 m_k^{\frac{-\lambda}{d+4}}$, Eq. 39 means:

$$\hat{p}_k(\mathbf{z}) = \frac{\hat{g}_k(\mathbf{z})\hat{\pi}_k}{\sum_{k'} \hat{g}_{k'}(\mathbf{z})\hat{\pi}_{k'}} \geq \frac{g_k(\mathbf{z})\pi_k - \epsilon_{k,2} - g_k(\mathbf{z})\epsilon_1}{\bar{g}(\mathbf{z}) + \sum_{k'} [\epsilon_{k',2} + g_{k'}(\mathbf{z})\epsilon_1]} \quad (40)$$

$$= \frac{g_k(\mathbf{z})\pi_k - \epsilon_{k,2} - g_k(\mathbf{z})\epsilon_1}{\bar{g}(\mathbf{z})} \frac{1}{1 + \frac{\sum_{k'} [\epsilon_{k',2} + g_{k'}(\mathbf{z})\epsilon_1]}{\bar{g}(\mathbf{z})}} \quad (41)$$

$$\geq \frac{g_k(\mathbf{z})\pi_k - \epsilon_{k,2} - g_k(\mathbf{z})\epsilon_1}{\bar{g}(\mathbf{z})} \left(1 - \frac{\sum_{k'} [\epsilon_{k',2} + g_{k'}(\mathbf{z})\epsilon_1]}{\bar{g}(\mathbf{z})}\right) \quad (42)$$

$$\geq p_k(\mathbf{z}) - \frac{\epsilon_{k,2} + g_k(\mathbf{z})\epsilon_1}{\bar{g}(\mathbf{z})} - \frac{\sum_{k'} [\epsilon_{k',2} + g_{k'}(\mathbf{z})\epsilon_1]}{\bar{g}(\mathbf{z})} \quad (43)$$

Similarly,

$$\hat{p}_k(\mathbf{z}) \leq \frac{g_k(\mathbf{z})\pi_k + \epsilon_{k,2} + g_k(\mathbf{z})\epsilon_1}{\bar{g}(\mathbf{z})} \frac{1}{1 - \frac{\sum_{k'} [\epsilon_{k',2} + g_{k'}(\mathbf{z})\epsilon_1]}{\bar{g}(\mathbf{z})}} \quad (44)$$

$$\leq \left(p_k(\mathbf{z}) + \frac{\epsilon_{k,2} + g_k(\mathbf{z})\epsilon_1}{\bar{g}(\mathbf{z})}\right) \left(1 + 2 \frac{\sum_{k'} [\epsilon_{k',2} + g_{k'}(\mathbf{z})\epsilon_1]}{\bar{g}(\mathbf{z})}\right) \quad (45)$$

$$\leq p_k(\mathbf{z}) + \frac{\epsilon_{k,2} + g_k(\mathbf{z})\epsilon_1}{\bar{g}(\mathbf{z})} + \frac{3 \sum_{k'} [\epsilon_{k',2} + g_{k'}(\mathbf{z})\epsilon_1]}{\bar{g}(\mathbf{z})} \quad (46)$$

We can proceed from Eq.44 to 45 and from 45 to 46 when $\frac{\sum_{k'} [\epsilon_{k',2} + g_{k'}(\mathbf{z})\epsilon_1]}{\bar{g}(\mathbf{z})} \leq 0.5$, which is achievable for a large m (the smallest m_k , thus N) given any \mathbf{z} as long as $\bar{g}(\mathbf{z}) > 0$.

With Eq. 43 and 46, with probability $\geq 1 - K(e^{-B_1 m^{\frac{4-2\lambda}{d+4}}} + e^{-B_2 N \epsilon_1^2})$:

$$|p_k(\mathbf{z}) - \hat{p}_k(\mathbf{z})| \leq \frac{(3K+1)(\epsilon_{k,2} + g^+(\mathbf{z})\epsilon_1)}{\bar{g}(\mathbf{z})} \quad (47)$$

$$= \frac{(3K+1)(C_1 m_k^{\frac{-\lambda}{d+4}} + g^+(\mathbf{z})\epsilon_1)}{\bar{g}(\mathbf{z})} \quad (48)$$

If we let $\epsilon_1 = \Theta(m^{\frac{-\lambda}{d+4}})$ and merge the constants, we have, with probability $\geq 1 - K e^{-B m^{\frac{4-2\lambda}{d+4}}}$ (note that $N \geq Km$):

$$|p_k(\mathbf{z}) - \hat{p}_k(\mathbf{z})| \leq (3K+1)C m^{\frac{-\lambda}{d+4}} \quad (49)$$

$$\implies |\mathbf{p}(\mathbf{z}) - \hat{\mathbf{p}}(\mathbf{z})|_1 \leq K(3K+1)C m^{\frac{-\lambda}{d+4}} \quad (50)$$

with some constant C and B that depends on $\{g_k(\mathbf{z})\}_{k \in [K]}$.

A.5 PROOF OF THEOREM 3.4

If we assume g_k is α -Hölder continuous for all k then by Theorem 2 in Jiang (2017), there exists positive constant C' independent of b and m , such that the following holds with probability $\geq 1 - \frac{1}{m_k}$

$$\sup_{\mathbf{z}} |\hat{g}_k(\mathbf{z}) - g_k(\mathbf{z})| < C' \left(b^\alpha + \sqrt{\frac{\log m_k}{m_k b^d}} \right). \quad (51)$$

Furthermore, we assume that all the densities are bounded from below (see, for example, Section 3 in Gadat et al. (2016)). Denote $U := \max_k \sup_{\mathbf{z}} g_k(\mathbf{z})$ and $L := \min_k \inf_{\mathbf{z}} g_k(\mathbf{z})$.

We could replace $\epsilon_{k,2}$ in the previous section with $\epsilon_{k,2} = C_1 (b^\alpha + \sqrt{\frac{\log m_k}{m_k b^d}})$. Following similar steps leading towards Eq. 43 and Eq. 46, we have, with probability $\geq 1 - K(\frac{1}{m} + e^{-B_2 N \epsilon_1^2})$, for any \mathbf{z} :

$$|\hat{p}_k(\mathbf{z}) - p_k(\mathbf{z})| \leq \frac{(3K+1)(\epsilon_{k,2} + g^+(\mathbf{z})\epsilon_1)}{\bar{g}(\mathbf{z})} \quad (52)$$

$$\leq \frac{(3K+1)}{L} \left(C_1 (b^\alpha + \sqrt{\frac{\log m}{m b^d}}) + U \epsilon_1 \right) \quad (53)$$

Note that we still need $\frac{\sum_{k'} [\epsilon_{k'} \cdot 2 + g_{k'}(\mathbf{z}) \epsilon_1]}{\bar{g}(\mathbf{z})} \leq 0.5$, which is satisfied as N increases because $g_k(\mathbf{z}) \geq L$. Now, we let $b = \Theta\left(\left(\frac{\log m}{m}\right)^{\frac{1}{d+2\alpha}}\right)$, and $\epsilon_1 = \Theta\left(\left(\frac{\log m}{m}\right)^{\frac{\alpha}{d+2\alpha}}\right)$, we have with probability $\geq 1 - K(m^{-1} + e^{-Bm^{\frac{d}{d+2\alpha}} (\log m)^{\frac{2\alpha}{d+2\alpha}}}) = 1 - K(m^{-1} + m^{-B \frac{2\alpha}{d+2\alpha}} m^{\frac{d}{d+2\alpha}})$:

$$|\hat{p}_k(\mathbf{z}) - p_k(\mathbf{z})| \leq (3K + 1)C \left(\frac{\log m}{m}\right)^{\frac{\alpha}{d+2\alpha}}. \quad (54)$$

Finally, with probability $\geq 1 - K(m^{-1} + m^{-B \frac{2\alpha}{d+2\alpha}} m^{\frac{d}{d+2\alpha}})$, for any \mathbf{q} in Δ^{K-1} :

$$\sup_{\mathbf{z}: \hat{\mathbf{p}}(\mathbf{z})=\mathbf{q}} |\mathbb{P}\{Y = k | \hat{\mathbf{p}}(\mathbf{z}) = \mathbf{q}\} - q_k| = \sup_{\mathbf{z}: \hat{\mathbf{p}}(\mathbf{z})=\mathbf{q}} |p_k(\mathbf{z}) - \hat{p}_k(\mathbf{z})| \leq \sup_{\mathbf{z}} |p_k(\mathbf{z}) - \hat{p}_k(\mathbf{z})| \leq (3K + 1)C \left(\frac{\log m}{m}\right)^{\frac{\alpha}{d+2\alpha}}. \quad (55)$$

B THEORETICAL ANALYSIS OF EQUAL-SIZED STRATIFIED SAMPLING IN TRAINING

We adopted equal-sized stratified sampling to facilitate efficient training. Here we provide some theoretical justification of this choice.

After fixing a x_0 whose label y_0 is the prediction target, the problem is essentially estimating $\frac{\mu_k p_k}{\sum_{k'} \mu_{k'} p_{k'}}$ for all k , where p_k denotes the frequency of class k in the population⁷ and μ_k denotes $\mathbb{E}[\phi(X, x_0) | Y = k]$. Note that we know p_k , but not μ_k , since p_k is fixed for our training set, but μ_k depends on x_0 and Π , which is what we are training. Suppose we can afford to use M samples in total to make the prediction, the question is: How do we distribute these M samples to different classes?

What sampling method to use will depend on many factors, although a stratified sampling strategy tends to be more efficient in sample size. The sampling method we use (sample the same number of samples for each class k) intuitively will improve the estimation quality of the rarer class. Here, we will elaborate why we chose this sampling method, the assumptions behind it, and why it helps training.

Denoting $S_k = \mu_k p_k$ and $S_{-k} = \sum_{k' \neq k} \mu_{k'} p_{k'}$, we can apply Taylor expansion to get an approximation of the variance⁸:

$$\text{Var}\left(\frac{S_k}{S_{-k} + S_k}\right) \approx \frac{1}{\mathbb{E}[S_{-k} + S_k]^2} \text{Var}(S_k) - 2 \frac{\mathbb{E}[S_k]}{\mathbb{E}[S_{-k} + S_k]^3} \text{Cov}(S_k, S_{-k} + S_k) \quad (56)$$

$$+ \frac{\mathbb{E}[S_k]^2}{\mathbb{E}[S_{-k} + S_k]^4} \text{Var}(S_{-k} + S_k) \quad (57)$$

If we perform stratified sampling of any kind, then $\text{Cov}(S_k, S_{-k}) = 0$, and Eq. (57) becomes:

$$\text{Var}\left(\frac{S_k}{S_{-k} + S_k}\right) \approx \frac{1}{\mathbb{E}[S_{-k} + S_k]^2} \text{Var}(S_k) - 2 \frac{\mathbb{E}[S_k]}{\mathbb{E}[S_{-k} + S_k]^3} \text{Var}(S_k) \quad (58)$$

$$+ \frac{\mathbb{E}[S_k]^2}{\mathbb{E}[S_{-k} + S_k]^4} [\text{Var}(S_{-k}) + \text{Var}(S_k)] \quad (59)$$

$$= \frac{\mathbb{E}[S_k]^2}{\mathbb{E}[S_{-k} + S_k]^4} \left(\left[\frac{\mathbb{E}[S_{-k}]}{\mathbb{E}[S_k]} \right]^2 \text{Var}(S_k) + \text{Var}(S_{-k}) \right) \quad (60)$$

To further analyze Eq. (60) and gain more intuition, we make the following assumptions:

- For any $k' \neq y_0$, $\mu_{k'}$ has the same value denoted as μ_{-y_0} (and is smaller than μ_{y_0}). Intuitively, this is like considering a one-vs-rest classification problem, and we are just saying data from the same class will look more similar according to our kernel.

⁷In our case, this population is the large training set.

⁸Such a derivation could be found in <https://www.stat.cmu.edu/~hseltman/files/ratio.pdf>

- The standard deviation for a single observation is directly proportional to the mean. Namely, for all k , $\frac{\sqrt{\text{Var}(\phi(X, x_0)|Y = k)}}{\mathbb{E}[\phi(X, x_0)|Y = k]} \equiv r$ for a fixed number r .

If we assign m_k samples to estimate μ_k then we have $\text{Var}(S_k) = r^2 \frac{\mathbb{E}[S_k]^2}{m_k}$ and $\text{Var}(S_{-k}) = r^2 \frac{\mathbb{E}[S_{-k}]^2}{M - m_k}$, where $M = \sum_{k'=1}^K m_{k'}$ ($M \gg m_k$ when K is large). This transforms Eq. (60) into:

$$\text{Var}\left(\frac{S_k}{S_{-k} + S_k}\right) \approx \frac{\mathbb{E}[S_k]^2 \mathbb{E}[S_{-k}]^2}{\mathbb{E}[S_{-k} + S_k]^4} r^2 \left(\frac{1}{m_k} + \frac{1}{M - m_k}\right) = C \left(\frac{1}{m_k} + \frac{1}{M - m_k}\right) \quad (61)$$

where C is a constant that does not depend on m_k .

Without prior information, it is natural to assume C is class-independent (or at least relatively constant across classes). Now, if our goal is to minimize the average variance, by Cauchy-Schwartz inequality we have:

$$\sum_{k=1}^K \frac{1}{m_k} \geq \frac{K^2}{M} \quad (62)$$

$$\sum_{k=1}^K \frac{1}{M - m_k} \geq \frac{K^2}{(K - 1)M} \quad (63)$$

The equality in both cases is achieved if and only if $m_k \equiv \frac{M}{K}$ for all k . This means, to minimize the average variance $\frac{C}{K} \sum_{k=1}^K \left(\frac{1}{m_k} + \frac{1}{M - m_k}\right)$, we need to choose m_k to be the same for all class k .

It is worth noting that the discussion above is about training (and how to get better estimation therein). This is not referring to errors of the final Π . Given enough time, different ways to sample data lead to similar performance.

C ADDITIONAL EXPERIMENTAL DETAILS

C.1 DATASETS

This section provides more detail on the healthcare datasets, which might be less familiar to readers.

IIIC (Jing et al., 2021; Ge et al., 2021) is an electroencephalography (EEG) dataset from the Massachusetts General Hospital EEG Archive. It is collected for the purpose of automated ictal-interictal-injury-continuum (IIIC) detection/monitoring. IIIC patterns include seizure and seizure-like patterns designated Lateralized Periodic Discharges (LPDs), Generalized Periodic Discharges (GPDs), Lateralized Rhythmic Delta Activity (LRDA), and Generalized Rhythmic Delta Activity (GRDA)(Ge et al., 2021). The training data has been enriched with “label spreading” (Ge et al., 2021), whereas the test (and calibration) data consists of only labels from medical experts. To improve stability (because IIIC labeling is a challenging task for even experts), any sample with less than 3 labels are dropped. The majority label is then used as the truth for the test and calibration ses. For more details on how the data was collected and labeled, please refer to Jing et al. (2021); Ge et al. (2021).

ISRUC (Khalighi et al., 2016) is a public polysomnographic (PSG) dataset for the sleep staging task. It has three groups of data, with the first group having the most data and most widely used. The (group 1) dataset contains 100 subjects with one recording session per subject. Every 30 second of the recording is considered an “epoch” and is rated independently by two human experts. We use the label from the first expert as the gold label. The five classes of ISRUC correspond to five different stages of sleep, including Rapid Eye Movement (REM), Non-REM Stage 1 (N1), Non-REM Stage 2 (N2), Non-REM Stage 3 (N3), and Wake (Wake). For more details, please refer to Khalighi et al. (2016).

PhysioNet Challenge 2017 (PN2017) (Clifford et al., 2017; Goldberger et al., 2000) is a public (upon request) electrocardiogram (ECG) dataset for ECG rhythm classification. The ECG recordings are sampled at 300Hz. The original dataset contains four classes: Normal sinus rhythm (N), Atrial Fibrillation (AF), Other cardiac rhythms (O) and Noise segment. Among these patterns, AF is an abnormal heart rhythm, and is the “important class”. We used the same processing method as Hong et al. (2019), which cuts one segment into several shorter segments with data augmentation during the training phase.

A summary of the classes can be found below in Table 7.

Table 7: Additional information about the healthcare datasets used in this paper.

Dataset	Name	IIIC		Name	ISRUC		Name	PN2017	
		Train	Cal+Test		Train	Cal+Test		Train	Cal+Test
Class 0	Other	42228	6852	Wake	14325	6433	Normal	8877	2893
Class 1	Seizure	3305	549	N1	7589	3798	Other	4524	1579
Class 2	LPD	17338	7589	N2	19501	8505	AF	1345	449
Class 3	GPD	16983	9737	N3	12012	5254	Noisy	341	145
Class 4	LRDA	12515	5946	REM	8414	3452	–	–	–
Class 5	GRDA	11449	5067	–	–	–	–	–	–

Data Licenses and Consent:

- **ISRUC**: We could not find the license. Per Khalighi et al. (2016), “All patients referred were submitted to an initial briefing with the support of an informed consent document. The ethics committee of CHUC approved the use of the data of the referred patients as anonymous for the research purposes”.
- **PN2017**: The license is Open Data Commons Attribution License v1.0. The dataset is donated by AliveCor.
- **IIIC**: We could not find the license. Per Jing et al. (2021) “the local IRB waived the requirement for informed consent for this retrospective analysis of EEG data”.
- **CIFAR-100/CIFAR-10**: We could not find the license. They are publicly available.
- **SVHN**: Under CC0: Public Domain license. It is publicly available.

C.2 BASELINE IMPLEMENTATION

- **Temperature Scaling:** We used the github repository accompanying Guo et al. (2017), https://github.com/gpleiss/temperature_scaling.
- **Dirichlet Calibration:** We used the code at https://github.com/dirichletcal/experiments_dnn.
- **Focal Loss (Mukhoti et al., 2020):** We used the loss function and the gamma schedule provided in https://github.com/torrvision/focal_calibration, and replaced our CrossEntropy loss function in all experiments during training.
- **Mutual-information-maximization-based Binning (I-Max):** We use the official github implementation <https://github.com/boschresearch/imax-calibration>. To normalize and get valid probability vectors, we used softmax on the log-odds given by I-Max.
- **Gaussian Process Calibration:** We use the official github implementation <https://github.com/JonathanWenger/pycalib>.
- **Splines-based Calibration:** We use the official github implementation <https://github.com/kartikgupta-at-anu/spline-calibration>.
- **Intra Order-preserving Calibration:** We use the official github implementation <https://github.com/AmirooR/IntraOrderPreservingCalibration>.
- **MMCE:** We use the official github implementation <https://github.com/aviralkumar2907/MMCE> with additional temperature scaling on the calibration set as suggested in the original paper.

C.3 TRAINING DETAILS

For CIFAR-10, CIFAR-100, SVHN, and ISRUC, the models are trained for 50 epochs, using a one-cycle Cosine scheduler with 3 warm-up and 10 cool-down epochs (the other parameters are default in `timm`). The exact ViT and Mixer are `vit_base_patch16_224_in21k` and `mixer_b16_224_in21k` implemented and pretrained by `timm`. For PN2017, the number of epochs is 100, and we use a `ReduceLRonPlateau` scheduler that halves the learning rate with the patience parameter set to 10 epochs. We use a batch size of 128, SGD optimizer and weight decay rate of $1e-4$. For IIIC dataset, we use a AdamW optimizer with a weight decay rate of $1e-5$, and no scheduler. The learning rates are $2e-4$ for CIFAR-10, CIFAR-100 and SVHN, $5e-3$ for ISRUC, $1e-2$ for PN2017 and $1e-3$ for IIIC. For all datasets except for IIIC, we used `LabelSmoothingCrossEntropy` in `timm` with `smoothing` being 0.1. For IIIC, since the original dataset contains pseudo-labels that form a distribution, we use a cross entropy loss. The experiments for the Focal baseline replace all loss functions with the proposed focal loss.

To train Π , we use an SGD optimizer with a learning rate of $4e-4$ for CIFAR-10, CIFAR-100, SVHN and IIIC, $1e-3$ for ISRUC and PN2017. We use `ReduceLRonPlateau` scheduler that halves the learning rate with the patience parameter set to 10 epochs, and trains for 100 epochs. Each epoch has a fixed number of 5000 batches (regardless of the size of the training set) and each batch consists of $B = 64$ prediction samples and a “background” set used to construct KDE with $m_k \equiv m = 20$ for all k . The exact details could be found in our code. Training time for the largest dataset (except for ImageNet), SVHN, is 3 hours for the base neural network, and 1 hour for Π on a machine with Nvidia RTX 3090 GPU. Inference time is much shorter.

C.4 ADDITIONAL EVALUATION METRICS

In this section, we compute the following variants of the evaluation metrics presented in the main text. The conclusion stays very similar across all methods.

- The static (equal-width bins) version of CECE, in Table 8.
- The static (equal-width bins) version of ECE, in Table 9.
- The multi-class version of Brier score, in Table 10. To be specific, the brier score in the main text is $\frac{1}{N} \sum_{i=1}^N (\hat{\mathbf{p}}_{k_i^*}(x_i) - \mathbb{1}\{y_i = k_i^*\})^2$ where $k_i^* = \arg \max_k \hat{\mathbf{p}}_k(x_i)$. The multi-class version of Brier score is $\frac{1}{NK} \sum_{i=1}^N \sum_{k=1}^K (\hat{\mathbf{p}}_k(x_i) - \mathbb{1}\{y_i = k\})^2$.
- NLL Loss, in Table 11.

Table 8: (Static) Class-wise ECE in 10^{-2} (\downarrow means lower=better). The best accuracy-preserving method is in **bold** ($p=0.01$). The otherwise lowest number is underscored. KCal almost always achieves the lowest class-wise ECE, while maintaining accuracy.

CECE \downarrow	UnCal	TS	DirCal	I-Max	Focal	Spline	IOP	GP	MMCE	KCal
IIIC (pat)	8.01±0.27	8.94±0.86	5.11±1.49	9.17±0.99	8.95±0.52	8.55±0.63	8.30±0.53	7.94±0.65	7.09±0.44	4.66±1.30
IIIC	7.89±0.02	8.96±0.50	2.13±0.13	8.77±0.24	8.76±0.02	8.41±0.23	7.97±0.26	7.51±0.24	6.66±0.26	2.04±0.27
ISRUC (pat)	4.51±0.25	4.68±0.77	4.19±0.89	8.65±0.99	9.24±0.20	4.67±0.46	4.59±0.59	4.63±0.42	4.06±0.35	3.84±1.22
ISRUC	4.53±0.02	5.18±0.79	2.73±0.38	9.29±0.86	9.07±0.02	4.75±0.16	4.69±0.37	4.71±0.25	4.07±0.21	1.93±0.27
PN2017	12.20±0.07	12.32±0.19	4.04±0.54	9.70±1.19	16.70±0.10	8.42±0.73	12.10±0.37	12.20±0.07	12.20±0.32	3.83±1.27
C10 (ViT)	3.42±0.01	1.39±0.08	1.25±0.08	1.15±0.06	5.19±0.03	1.36±0.06	1.25±0.07	1.23±0.06	1.52±0.22	1.18±0.08
C10 (Mixer)	3.36±0.02	2.11±0.11	1.64±0.08	1.76±0.24	7.02±0.03	1.71±0.09	1.78±0.10	1.75±0.10	1.95±0.27	1.59±0.06
C100 (ViT)	6.33±0.05	6.43±0.29	5.44±0.14	5.96±0.21	6.07±0.05	5.16±0.17	5.58±0.14	5.54±0.09	5.30±0.22	5.06±0.11
C100 (Mixer)	5.60±0.05	6.75±0.25	5.87±0.20	6.64±0.29	6.08±0.06	5.56±0.13	6.09±0.32	5.80±0.14	6.15±0.21	5.16±0.07
SVHN (ViT)	3.50±0.01	2.56±0.58	1.40±0.06	2.98±0.22	6.11±0.02	1.51±0.07	1.47±0.07	1.51±0.05	1.63±0.11	1.46±0.08
SVHN (Mixer)	3.36±0.02	3.38±0.67	1.39±0.11	3.00±0.16	5.79±0.02	1.66±0.07	1.54±0.06	1.58±0.06	1.73±0.09	1.57±0.11
ImageNet	3.70±0.03	3.99±0.07	6.11±0.22	3.29±0.21	–	2.80±0.07	2.93±0.16	3.05±0.08	–	2.40±0.04

Table 9: (Static) ECE in 10^{-2} (\downarrow means lower=better). The best accuracy-preserving method is in **bold** ($p=0.01$). KCal is usually on par or better than the best baseline.

ECE \downarrow	UnCal	TS	DirCal	I-Max	Focal	Spline	IOP	GP	MMCE	KCal
IIIC (pat)	9.18±1.08	4.95±2.77	2.87±1.62	10.56±4.05	7.37±0.53	4.54±2.07	4.56±2.15	3.84±1.63	6.34±3.30	4.28±1.42
IIIC	9.13±0.04	4.42±1.53	1.22±0.17	10.17±0.81	7.10±0.04	3.08±0.65	3.44±0.38	1.68±0.55	4.78±2.26	2.55±0.61
ISRUC (pat)	3.60±0.32	2.70±1.56	2.91±1.02	8.82±1.41	14.95±0.40	1.99±0.36	2.40±1.43	1.94±0.62	2.09±0.97	2.74±1.29
ISRUC	3.46±0.06	3.81±1.67	2.20±0.68	9.58±1.26	14.76±0.05	1.48±0.55	2.69±0.94	2.04±0.76	2.08±1.06	1.34±0.41
PN2017	17.10±0.14	17.34±0.42	5.46±0.66	8.97±1.85	24.65±0.13	6.10±2.22	16.55±2.03	17.13±0.15	13.21±1.08	4.56±1.41
C10 (ViT)	9.17±0.05	0.76±0.11	0.44±0.08	0.61±0.06	7.19±0.06	0.49±0.10	0.38±0.05	0.28±0.07	0.65±0.15	0.41±0.10
C10 (Mixer)	9.06±0.05	1.11±0.12	0.51±0.05	1.04±0.17	12.54±0.06	0.48±0.08	0.56±0.12	0.34±0.06	1.01±0.40	0.65±0.09
C100 (ViT)	11.65±0.14	2.81±0.44	0.77±0.12	3.39±0.23	9.98±0.09	1.07±0.24	1.24±0.27	0.92±0.12	1.21±0.36	1.58±0.33
C100 (Mixer)	13.71±0.15	3.18±0.35	1.17±0.26	4.82±0.25	14.36±0.20	1.20±0.35	1.82±0.72	1.15±0.22	2.14±0.49	3.11±0.48
SVHN (ViT)	10.11±0.05	2.44±2.72	0.61±0.09	2.08±0.18	12.17±0.08	0.64±0.14	0.55±0.11	0.61±0.10	0.66±0.15	0.71±0.13
SVHN (Mixer)	10.30±0.04	3.19±2.55	0.57±0.08	2.21±0.10	11.09±0.06	0.67±0.13	0.49±0.10	0.62±0.08	0.69±0.21	0.74±0.11
ImageNet	3.06±0.13	3.26±0.13	4.26±0.74	8.05±0.32	–	1.13±0.15	1.38±0.46	0.95±0.16	–	1.30±0.28

Table 10: Brier Score (multi-class) in 10^{-2} (\downarrow means lower=better). The best accuracy-preserving methods are in **bold** ($p=0.01$).

Brier \downarrow	UnCal	TS	DirCal	I-Max	Focal	Spline	IOP	GP	MMCE	KCal
IIIC (pat)	9.23±0.18	9.11±0.31	8.13±0.26	9.22±0.44	9.69±0.20	9.05±0.25	9.07±0.27	9.01±0.24	9.13±0.25	8.38±0.36
IIIC	9.25±0.01	9.10±0.06	7.86±0.02	9.17±0.05	9.68±0.00	9.00±0.01	9.05±0.03	8.95±0.03	9.07±0.06	7.40±0.04
ISRUC (pat)	6.84±0.17	6.83±0.17	6.83±0.21	7.15±0.21	7.97±0.14	6.79±0.17	6.82±0.18	6.80±0.17	6.59±0.14	6.67±0.18
ISRUC	6.95±0.02	6.97±0.06	6.66±0.04	7.31±0.11	8.07±0.01	6.90±0.02	6.94±0.04	6.90±0.03	6.68±0.02	6.30±0.03
PN2017	14.92±0.02	14.97±0.11	12.85±0.09	14.03±0.20	17.64±0.01	13.78±0.13	14.84±0.24	14.92±0.02	15.26±0.17	12.81±0.13
C10 (ViT)	0.27±0.01	0.18±0.01	0.16±0.01	0.17±0.01	0.31±0.01	0.16±0.01	0.16±0.01	0.16±0.01	0.18±0.01	0.15±0.01
C10 (Mixer)	0.39±0.01	0.30±0.01	0.30±0.01	0.30±0.02	0.74±0.01	0.29±0.01	0.29±0.01	0.28±0.01	0.30±0.03	0.28±0.01
C100 (ViT)	0.14±0.00	0.12±0.00	0.12±0.00	0.12±0.00	0.14±0.00	0.12±0.00	0.12±0.00	0.12±0.00	0.11±0.00	0.11±0.00
C100 (Mixer)	0.21±0.00	0.19±0.00	0.18±0.00	0.19±0.00	0.23±0.00	0.18±0.00	0.18±0.00	0.18±0.00	0.17±0.00	0.18±0.00
SVHN (ViT)	0.76±0.01	0.65±0.04	0.62±0.01	0.65±0.01	0.95±0.01	0.62±0.01	0.62±0.01	0.62±0.01	0.54±0.00	0.55±0.01
SVHN (Mixer)	0.77±0.01	0.68±0.05	0.62±0.01	0.66±0.01	0.97±0.01	0.63±0.01	0.63±0.01	0.63±0.01	0.68±0.01	0.60±0.01
ImageNet	0.03±0.00	0.03±0.00	0.03±0.00	0.03±0.00	–	0.03±0.00	0.03±0.00	0.03±0.00	–	0.03±0.00

Table 11: NLL (\downarrow means lower=better). The best accuracy-preserving methods are in **bold** ($p=0.01$).

NLL \downarrow	UnCal	TS	DirCal	I-Max	Focal	Spline	IOP	GP	MMCE	KCal
IIIC (pat)	1.09±0.02	1.08±0.05	0.97±0.05	1.11±0.07	1.11±0.03	1.07±0.03	1.07±0.04	1.06±0.03	1.07±0.03	1.00±0.05
IIIC	1.09±0.00	1.08±0.01	0.92±0.00	1.10±0.01	1.11±0.00	1.06±0.00	1.06±0.00	1.05±0.00	1.06±0.01	0.87±0.01
ISRUC (pat)	0.63±0.02	0.62±0.02	0.62±0.02	0.69±0.03	0.72±0.01	0.61±0.02	0.62±0.02	0.61±0.02	0.60±0.02	0.61±0.02
ISRUC	0.64±0.00	0.63±0.01	0.60±0.00	0.71±0.02	0.73±0.00	0.63±0.00	0.63±0.00	0.62±0.00	0.61±0.00	0.57±0.00
PN2017	1.00±0.00	1.00±0.00	0.86±0.01	0.96±0.02	1.19±0.00	0.95±0.01	0.99±0.02	1.00±0.00	1.04±0.03	0.86±0.01
C10 (ViT)	0.12±0.00	0.05±0.01	0.03±0.00	0.04±0.00	0.10±0.00	0.04±0.00	0.03±0.00	0.03±0.00	0.05±0.00	0.03±0.00
C10 (Mixer)	0.15±0.00	0.07±0.01	0.06±0.00	0.07±0.00	0.20±0.00	0.06±0.00	0.06±0.00	0.06±0.00	0.07±0.02	0.06±0.00
C100 (ViT)	0.38±0.00	0.29±0.01	0.28±0.01	0.32±0.01	0.36±0.00	0.28±0.01	0.28±0.01	0.27±0.01	0.25±0.01	0.27±0.00
C100 (Mixer)	0.54±0.01	0.43±0.01	0.43±0.01	0.47±0.01	0.54±0.01	0.43±0.01	0.43±0.01	0.42±0.01	0.39±0.01	0.44±0.01
SVHN (ViT)	0.23±0.00	0.16±0.02	0.15±0.00	0.17±0.00	0.26±0.00	0.15±0.00	0.15±0.00	0.15±0.00	0.13±0.00	0.13±0.00
SVHN (Mixer)	0.23±0.00	0.19±0.03	0.15±0.00	0.18±0.00	0.26±0.00	0.16±0.00	0.15±0.00	0.15±0.00	0.16±0.00	0.15±0.00
ImageNet	0.84±0.01	0.83±0.01	0.90±0.02	0.87±0.02	–	0.77±0.01	0.75±0.01	0.75±0.01	–	0.87±0.01

C.5 RELIABILITY DIAGRAMS

Figure 3, 4, and 5 are the reliability diagrams for the IIC, ISRUC and PN2017 dataset, respectively. We keep only bins with at least 15 samples, because otherwise the “gap” is misleading due to small sample and big variance. The count of samples in each bin is plotted on the right axis (log-scale). The conclusion is similar. In all cases, TS seems to calibrate the overall ECE but fails on some classes. DirCal tends to improve on all classes, but KCal usually closes the gap between actual frequency and the prediction further.

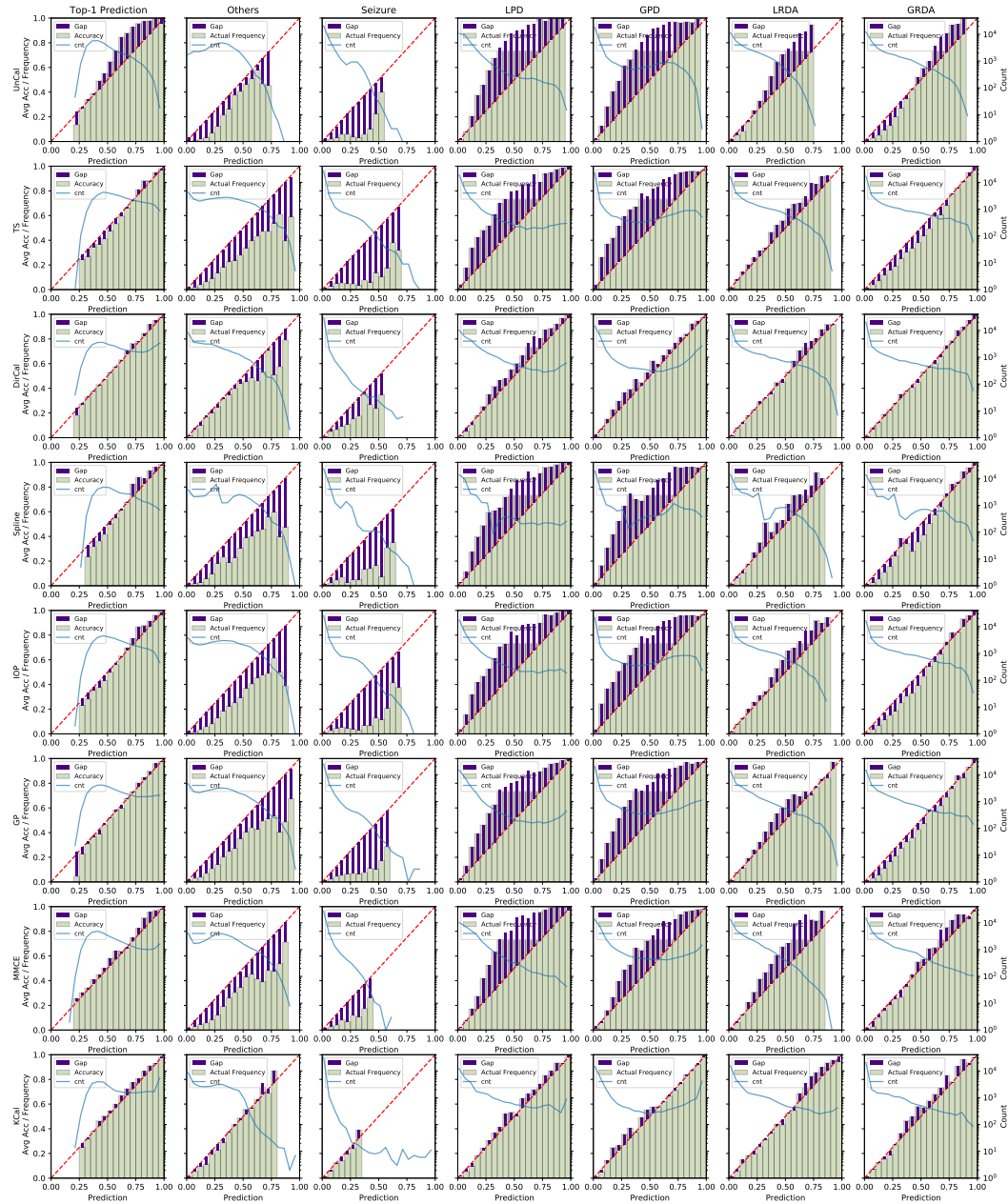


Figure 3: Reliability diagrams for the IIC dataset.

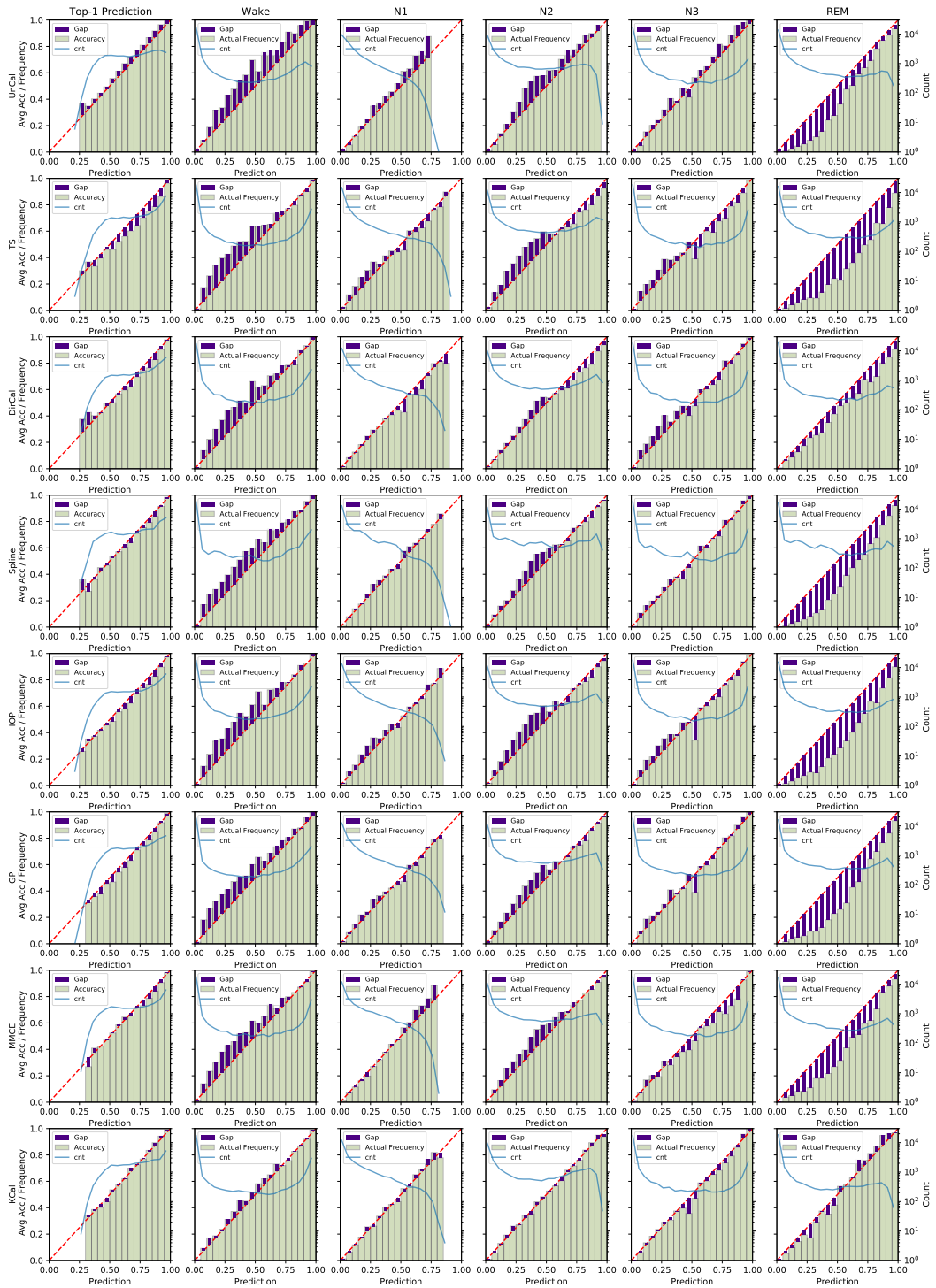


Figure 4: Reliability diagrams for the ISRUC dataset.

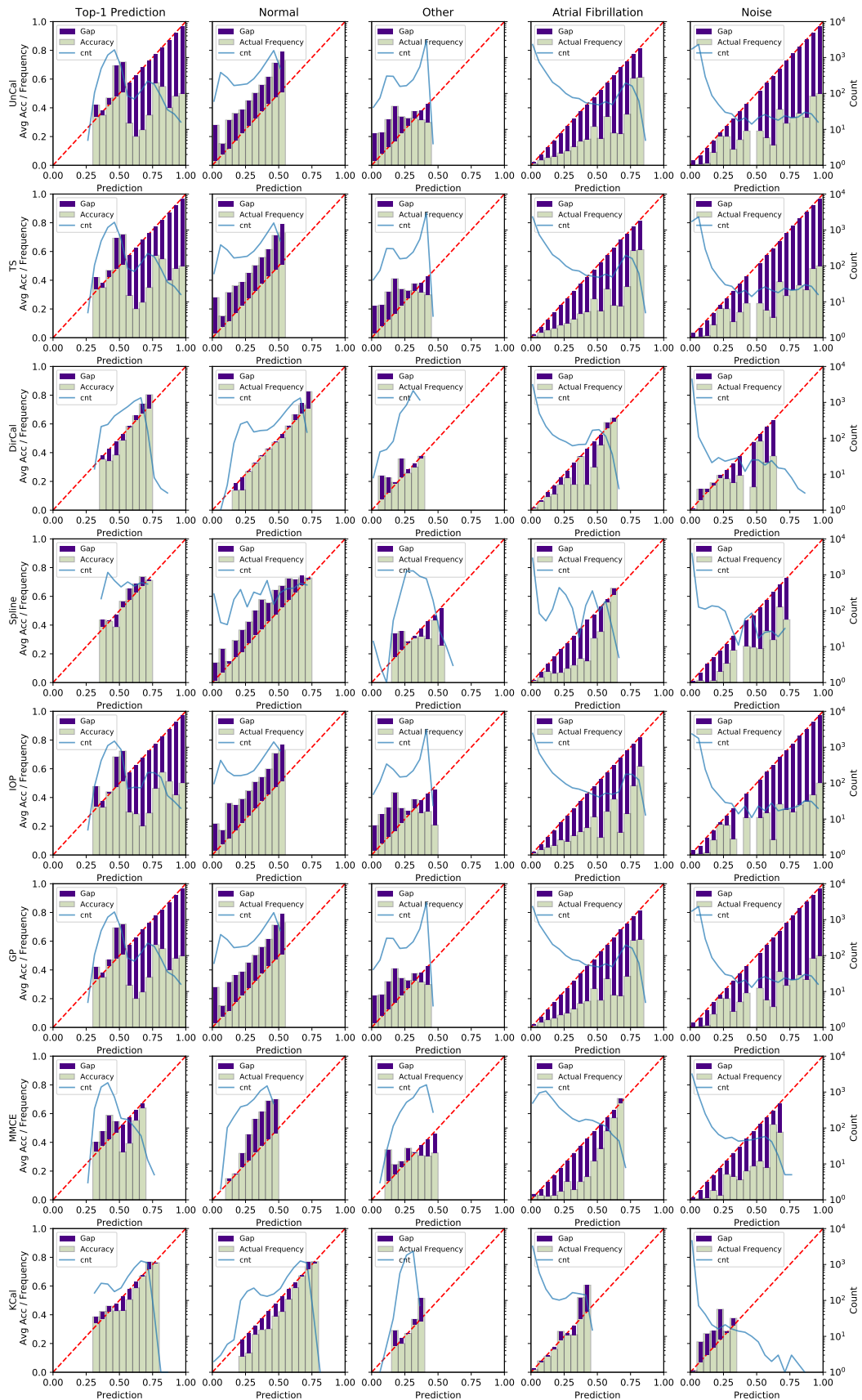
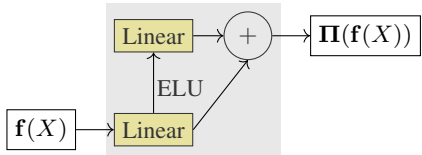


Figure 5: Reliability diagrams for the PN2017 dataset.

Figure 6: Structure of the learnable projection Π (in gray).

D ABLATION STUDY: LINEAR PROJECTION

A natural first architecture to try for Π is a simple linear layer. It is however not clear whether a linear projection can learn the best metric space due to its simplicity. We introduced a mild complexity by having two layers in Π , yet the skip connection should help it learn well when a linear projection is the most desirable as well. We empirically compared both versions: KCal, with the architecture showed in Figure 6, and KCal-Linear, which only uses one linear layer with the same output dimension (d). Both Π normalized $f(\cdot)$ automatically with a Batch Normalization layer. The results are in Table 12. As we can see, KCal is generally better than the linear version, but the gap is generally small. The additional computation time is smaller than 1x the computation time for KCal-Linear, because the second layer has only d^2 parameters rather than hd in the first layer ($h > d$). Both have negligible computation overhead compared with calling f (see Appendix F).

Table 12: Comparison between the architecture described in Figure 6 (KCal) and a simple linear projection with the same input and output dimensions (KCal-Linear). On average, KCal adapts to different datasets and architectures better than (KCal-Linear), although the performance is generally similar.

	Accuracy \uparrow		CECE \downarrow		ECE \downarrow		Brier \downarrow	
	KCal	KCal-Lienar	KCal	KCal-Lienar	KCal	KCal-Lienar	KCal	KCal-Lienar
IIC(pat)	61.67\pm2.22	61.51 \pm 2.46	4.68\pm1.27	4.68 \pm 1.41	4.34\pm1.35	4.48 \pm 1.99	19.33 \pm 0.78	19.28\pm0.82
IIC	66.32\pm0.21	65.59 \pm 0.20	2.03\pm0.26	2.08 \pm 0.23	2.62\pm0.59	3.12 \pm 0.68	17.54\pm0.10	17.88 \pm 0.09
ISRUC(pat)	76.13\pm0.89	76.02 \pm 1.08	3.82\pm1.24	3.96 \pm 1.34	2.78\pm1.25	2.87 \pm 1.53	14.97\pm0.29	15.04 \pm 0.30
ISRUC	77.45\pm0.16	77.19 \pm 0.19	1.90\pm0.28	2.01 \pm 0.31	1.36\pm0.41	1.69 \pm 0.46	14.28\pm0.08	14.37 \pm 0.08
PN2017	60.36\pm0.61	60.15 \pm 0.56	4.25 \pm 1.26	4.21\pm1.26	4.78\pm1.48	5.41 \pm 1.14	22.56\pm0.28	22.69 \pm 0.32
C10 (ViT)	98.98\pm0.09	98.96 \pm 0.07	0.74 \pm 0.07	0.72\pm0.06	0.40 \pm 0.05	0.31\pm0.06	0.75\pm0.05	0.75 \pm 0.05
C10 (Mixer)	98.14\pm0.06	98.12 \pm 0.09	1.17\pm0.10	1.18 \pm 0.07	0.59\pm0.09	0.61 \pm 0.13	1.34\pm0.04	1.34 \pm 0.05
C100 (ViT)	92.37 \pm 0.15	92.47\pm0.14	4.32\pm0.10	4.37 \pm 0.08	1.50 \pm 0.32	1.43\pm0.33	5.01 \pm 0.08	4.93\pm0.08
C100 (Mixer)	87.55 \pm 0.16	88.00\pm0.24	4.62\pm0.10	4.73 \pm 0.12	3.07 \pm 0.49	2.78\pm0.45	7.61 \pm 0.09	7.39\pm0.07
SVHN (ViT)	96.42\pm0.05	96.36 \pm 0.06	1.23\pm0.10	1.32 \pm 0.08	0.64\pm0.12	0.65 \pm 0.09	2.49\pm0.03	2.49 \pm 0.03
SVHN (Mixer)	96.10 \pm 0.04	96.13\pm0.04	1.40\pm0.08	1.49 \pm 0.08	0.73 \pm 0.10	0.61\pm0.09	2.68\pm0.03	2.69 \pm 0.03

E ABLATION STUDY: USING THE CLASSIFICATION LOGITS

We empirically compared using the penultimate-layer embeddings and the predicted logits in Table 13. As we can see, KCal is generally better than the alternative that uses the logits.

Table 13: Comparison between using the penultimate layer embedding vs the prediction logits as the input to Π (KCal-Logits). Overall, KCal is significantly better than KCal-Logits, but KCal-Logits also has competitive performance.

	Accuracy \uparrow		CECE \downarrow		ECE \downarrow		Brier \downarrow	
	KCal	KCal-Logits	KCal	KCal-Logits	KCal	KCal-Logits	KCal	KCal-Logits
IIC(pat)	61.67\pm2.22	61.21 \pm 2.66	4.68 \pm 1.27	4.26\pm1.30	4.34 \pm 1.35	4.02\pm1.51	19.33 \pm 0.78	19.07\pm0.77
IIC	66.32\pm0.21	65.26 \pm 0.20	2.03\pm0.26	2.11 \pm 0.27	2.62\pm0.59	2.77 \pm 0.37	17.54\pm0.10	17.90 \pm 0.05
ISRUC(pat)	76.13\pm0.89	75.57 \pm 1.02	3.82\pm1.24	3.95 \pm 1.44	2.78 \pm 1.25	2.75\pm1.27	14.97\pm0.29	15.30 \pm 0.31
ISRUC	77.45\pm0.16	76.75 \pm 0.12	1.90\pm0.28	1.97 \pm 0.32	1.36\pm0.41	1.62 \pm 0.48	14.28\pm0.08	14.60 \pm 0.09
PN2017	60.36\pm0.61	59.99 \pm 0.56	4.25 \pm 1.26	4.13\pm1.22	4.78\pm1.48	5.18 \pm 0.96	22.56\pm0.28	22.64 \pm 0.34
C10 (ViT)	98.98\pm0.09	98.94 \pm 0.06	0.74\pm0.07	0.79 \pm 0.07	0.40\pm0.05	0.43 \pm 0.05	0.75\pm0.05	0.79 \pm 0.04
C10 (Mixer)	98.14\pm0.06	98.11 \pm 0.06	1.17\pm0.10	1.21 \pm 0.07	0.59 \pm 0.09	0.54\pm0.06	1.34\pm0.04	1.37 \pm 0.04
C100 (ViT)	92.37\pm0.15	91.11 \pm 0.14	4.32\pm0.10	4.67 \pm 0.10	1.50\pm0.32	1.95 \pm 0.37	5.01\pm0.08	5.55 \pm 0.08
C100 (Mixer)	87.55\pm0.16	85.07 \pm 0.26	4.62\pm0.10	4.98 \pm 0.13	3.07\pm0.49	3.73 \pm 0.54	7.61\pm0.09	8.84 \pm 0.06
SVHN (ViT)	96.42\pm0.05	96.05 \pm 0.05	1.23\pm0.10	1.53 \pm 0.12	0.64\pm0.12	0.91 \pm 0.08	2.49\pm0.03	2.76 \pm 0.03
SVHN (Mixer)	96.10\pm0.04	95.90 \pm 0.05	1.40\pm0.08	1.65 \pm 0.11	0.73\pm0.10	0.88 \pm 0.09	2.68\pm0.03	2.84 \pm 0.03

F ABLATION STUDY: EFFECT OF d

To investigate the effect of d , we tried $d = 8, 16, 32, 64$, and 128 and repeat the experiments. The performance and the inference time (overhead) can be found in Figure 7. The inference time depends on the size of the calibration set, which is specified in Section 4.

Generally speaking, we can only tell for sure that increasing d increases the overhead, although the overhead is always small compared with calling f . The effect on other metrics, including accuracy, ECE and CEC, is not monotonic, and the best d probably depends on many factors.

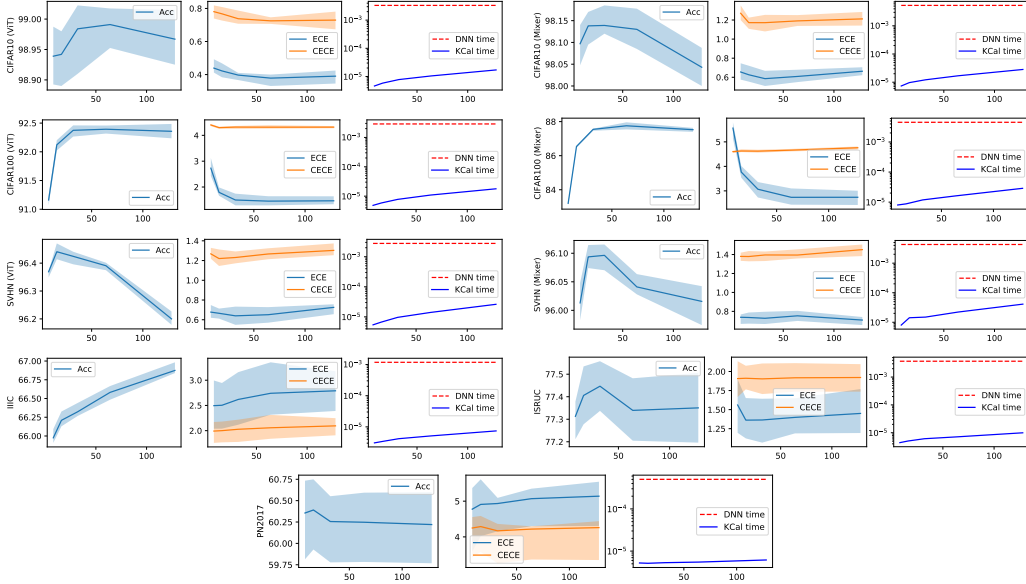


Figure 7: Change in performance and inference time if we we change d (the output embedding size of Π). “DNN time” refers to the average time running f for one input x , and “KCal time” refers to the average time transforming $f(x)$ to $\hat{p}(x)$ using KCal. For Accuracy, ECE and CECE, the unit is percentage. The band represents the median 50% among 10 experiments. For time, the unit is second. Performance is not always improving as d increases, but a larger d naturally leads to larger overhead. It is however worth noting that in all experiment, the overhead (“KCal time”) is negligible compared with the ‘DNN time’.

G COMPUTING BANDWIDTH

As suggested in the main text, although there is a bandwidth selection step that seemingly prevents KCal from efficiently updating predictions in an online manner, we could actually leverage Lemma 3.2 to compute b as opposed to actually performing cross-validation. To verify empirically that this is feasible in practice, we perform experiments where we vary the size of the calibration set, and plot the cross-validation-selected bandwidth b against the predicted value $\Theta(m^{-\frac{1}{d+4}})$. The results are in Figure 8.

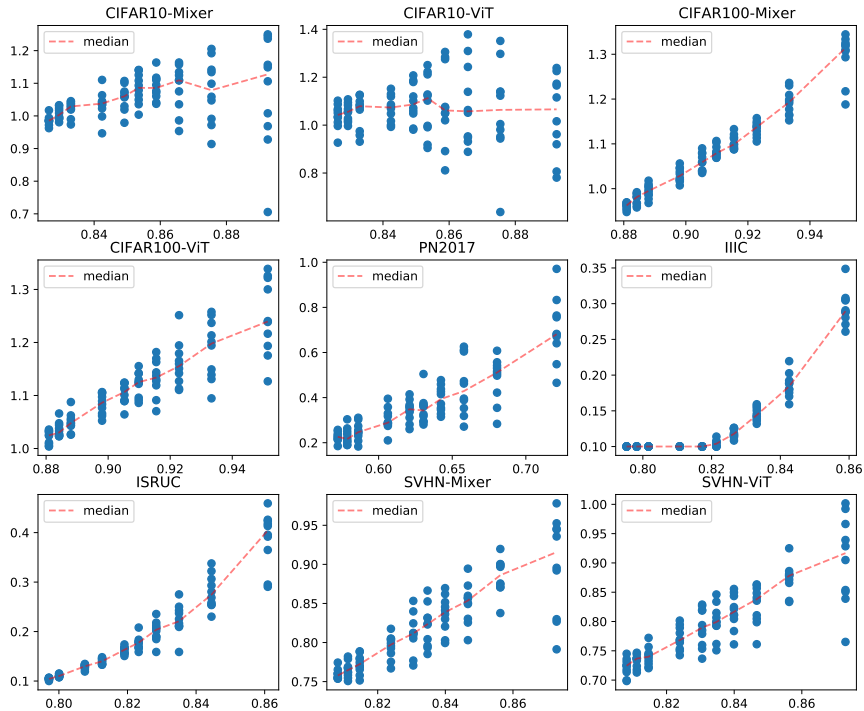


Figure 8: Empirically-selected bandwidth (b^*) on the y-axis, and predicted bandwidth ($\Theta(m^{-\frac{1}{d+4}})$) on the x-axis. For each calibration set size we have 10 experiments like in the main text, and we plot the scatter plot and median of the experiments. As expected, we see a nearly linear relationship for most data, except for IIIC, which exhibits a piece-wise linear pattern. This suggests that in practice, as new samples are added into the calibration set in an online manner, we could *compute* the bandwidth b and only re-do the cross validation sparingly.

If everything is perfect, we should see a linear relation in all plots, and we can use this relationship to compute b^* when we gradually add samples to the calibration set. It is clear that if we use the estimated constant in the $\Theta(\cdot)$ and the calibration set size (per class) m to set the bandwidth, we are still very close to the empirically selected value most of the time. In practice, this means that we only need to perform the actual cross validation occasionally, and predict the b^* in between. Note that from left to right, m decreases, so the optimal b^* increases and the variance increases greatly due to m being small. In practice, one might keep updating b^* using cross validation when m is small (and cross-validation takes very little time) and only compute b^* when m is already large.

While computation will give good estimates for b^* for most datasets, especially when m is large and the estimate of b^* is relatively stable (towards the left ends of plots), IIC (and ISRUC to some extent) seems to show two different slopes. As m increases, from right to left, b^* seems to first decrease, and then stop decreasing. While a detailed analysis for this are beyond the scope of this paper, there are a few possible reasons.

1. First, and most importantly, the optimal bandwidth derived in Lemma 3.2 is “best” for estimating the density, f_k (in Eq. (4), not $\mathbb{P}\{\cdot|X\}$). b^* is however chosen according to the log-loss of the KDE classifier. As a result, the formula should be more relevant when K is large and the difference between $\hat{p}_k(X)$ and $\mathbb{P}\{Y = k|X\}$ is essentially linear in $\hat{f}_k - f_k$ (as the denominator is much more accurate than the numerator). The experiment does support this point, since CIFAR100, with 100 classes, exhibits the clearest linear relationship.
2. Lemma 3.2 is not applicable if $f_{\Pi \circ f}$ violates the assumptions. For example, if f creates a discontinuity in the density, with a lot of data from different classes mapped to the same embedding. This means decreasing b might not decrease the bias term in Section A.2, and only increases variance. This could be what is happening in CIFAR10-ViT (with 99% accuracy) and in the left end of IIC: decreasing b might not improve log-loss as we have exhausted the discriminative power of f .

H BANDWIDTH SELECTION

In Section 3.4, we stated that we use Golden-Section search because we assume the cross entropy loss is convex in bandwidth b . While the convexity is expected from the bias-variance trade-off, we show in Figure 9 that this is indeed the case.

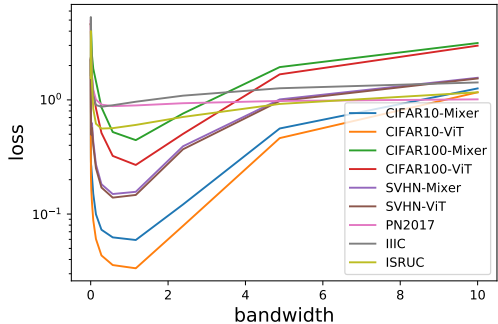


Figure 9: Change in cross validation loss used for the Golden-Section Search mentioned in Section 3.4 as a function of bandwidth. As we can see, the loss is indeed roughly convex in the bandwidth for all datasets.

I EFFECT OF $|\mathcal{S}_{CAL}|$

In Figure 10, we plot the accuracy, Brier score, CECE and ECE as a function of $|\mathcal{S}_{cal}|$ for different datasets. As expected, as $|\mathcal{S}_{cal}|$ increases, the performance of KCal increases and then stabilizes.

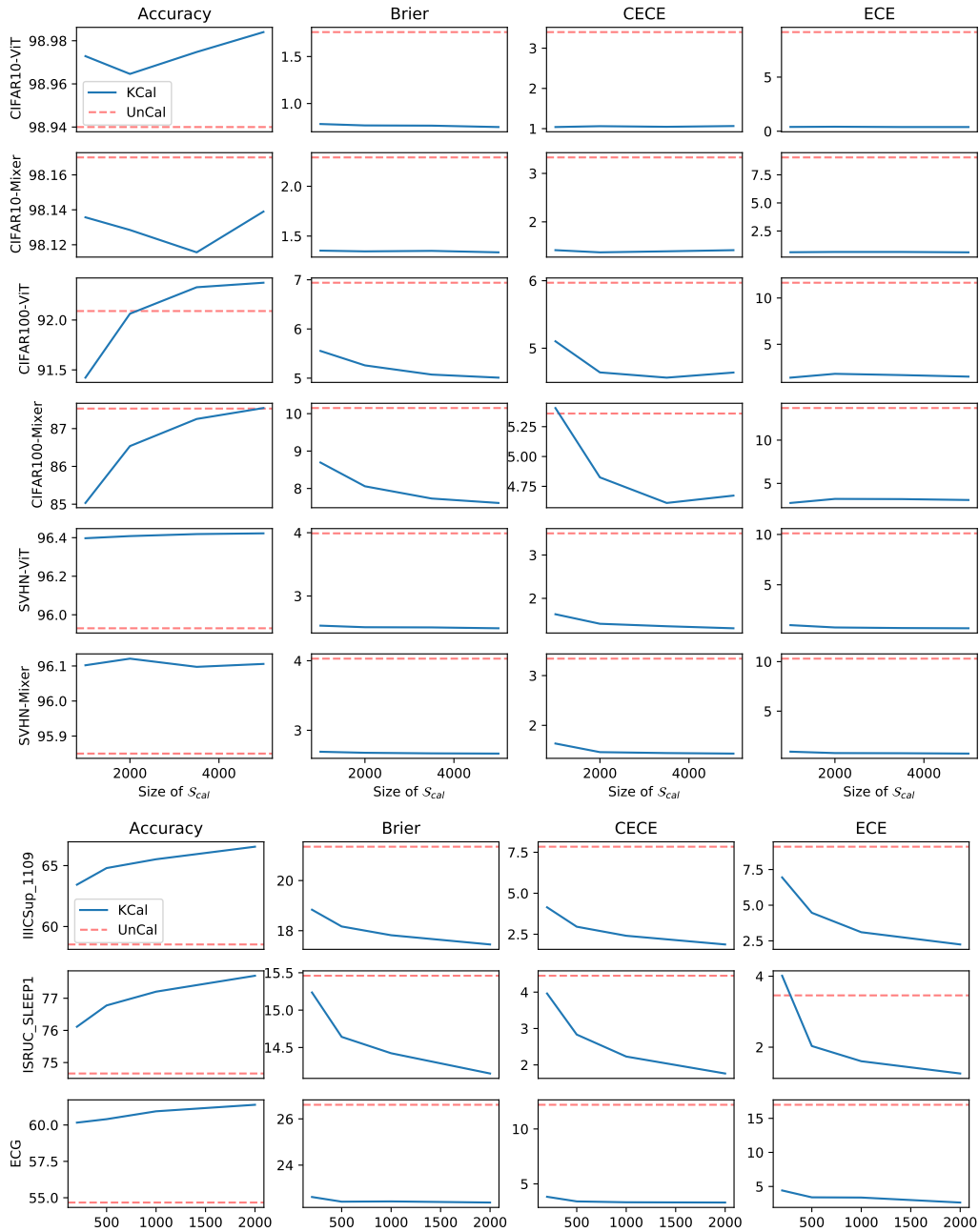


Figure 10: We change the size of S_{cal} and repeat the experiment for KCal. The red dashed line denotes UnCal. We see that, as expected, all metrics improves as the size of the calibration set increases, and the performance is generally stable.